Acta Pharmaceutica Sinica B 2026;16(1):574−595

Chinese Pharmaceutical Association
Institute of Materia Medica, Chinese Academy of Medical Sciences

Acta Pharmaceutica Sinica B

www.elsevier.com/locate/apsb
www.sciencedirect.com

ORIGINAL ARTICLE

Endogenic transferrin-targeted cell membrane-coated biomimetic lipo-complexes for efficient targeting and enhanced antitumor efficacy in orthotopic glioblastoma

Aihua Jin[a,b,c,†], Nuoya Wang[a,b,d,†], Yanhong Liu[a,b], Shuangqing Wang[a,b], Liqing Chen[a,b], Liming Gong[a,b], Wei Huang[a,b], Zhonggao Gao[a,b,*], Mingji Jin[a,b,*]

[a]*State Key Laboratory of Bioactive Substance and Function of Natural Medicines, Institute of Materia Medica, Chinese Academy of Medical Sciences and Peking Union Medical College, Beijing 100050, China*
[b]*Beijing Key Laboratory of Drug Delivery Technology and Novel Formulations, Institute of Materia Medica, Chinese Academy of Medical Sciences and Peking Union Medical College, Beijing 100050, China*
[c]*Department of Clinical Laboratory, Yanbian University Hospital, Yanji 133000, China*
[d]*Department of Pharmacy, Yanbian University, Yanji 133000, China*

Received 19 January 2025; received in revised form 23 April 2025; accepted 14 May 2025

KEY WORDS

Transferrin protein corona;
Cell membrane biomimetic nanoparticles;
Photodynamic therapy;
Glioblastoma;
Blood−brain barrier;
Brain targeting;
Hypoxia inhibition relief;
Immungentic cell death

Abstract Due to the invasive growth of glioblastomas (GBM) and their resistance to conventional chemotherapy, the efficacy of GBM treatment remains limited. Biomimetic BBB-penetrating hybrid nanovehicles, engineered through homologous cell membrane fusion between cancer cells and protein corona (PC)-mediated liposomes coated with cancer cell membranes, have been explored for brain-targeted drug delivery. In this study, T_{10} peptide-modified cell membrane-coated liposomes were used to construct an *in situ* transferrin (Tf) PC-mediated lipo-complex carrying a respiratory depressant agent (metformin, MET) and a photosensitizer (Chlorin, Ce6), creating a transferrin- and cancer cell-targeting delivery system (MET/Ce6@Lipo@CM@T_{10}). MET/Ce6@Lipo@CM@T_{10} possesses a spherical core −shell structure with uniform distribution while maintaining low systemic toxicity. Upon irradiation, MET/Ce6@Lipo@CM@T_{10} effectively inhibited cell proliferation and induced apoptosis *via* photodynamic therapy (PDT). Simultaneously, the loaded MET alleviated intracellular hypoxia caused by PDT, thereby enhancing anti-tumor efficacy. The establishment of an *in vitro* BBB model and 3D tumor

*Corresponding authors.
E-mail addresses: zggao@imm.ac.cn (Zhonggao Gao), jinmingji@imm.ac.cn (Mingji Jin).
[†]These authors made equal contributions to this work.
Peer review under the responsibility of Chinese Pharmaceutical Association and Institute of Materia Medica, Chinese Academy of Medical Sciences.

https://doi.org/10.1016/j.apsb.2025.08.019

spheroid experiments confirmed that MET/Ce6@Lipo@CM@T_{10} effectively crossed BBB and deeply accumulated within tumor tissues. As a result, in *in vivo* animal experiments, MET/Ce6@Lipo@CM@T_{10} significantly inhibited tumor growth, promoted tumor necrosis and apoptosis, and demonstrated systemic safety. In conclusion, MET/Ce6@Lipo@CM@T_{10} demonstrated enhanced PDT effects on GBM, and will provide new insights and methods for GBM treatment.

1. Introduction

Glioma, the most common aggressive brain malignancy, accounts for over 80% of central nervous system-related cancers[1,2] Glioblastoma (GBM), the most aggressive form of glioma, is highly invasive, making complete surgical resection difficult without impairing normal neurological function[3,4]. Consequently, the median survival time for GBM patients after diagnosis is less than 15 months, and the 5-year survival rate is only 5%[5]. Chemotherapy remains an essential component of GBM treatment, improving surgical outcomes[6]. However, it is associated with poor blood circulation, insufficient tumor penetration, and an inability to cross the blood−brain barrier (BBB)[7,8]. The BBB, a complex and selective biofilm composed of various cell types, prevents nearly all large-molecule drugs and over 98% of small-molecule drugs from entering the brain[9]. Overcoming the BBB to deliver chemotherapy drugs effectively for GBM treatment remains a critical challenge[10].

Biomimetic nanodelivery systems—such as those based on cells, cell membrane (CM), extracellular vesicles, viral vectors, and endogenous proteins extracted from organisms—offer promising solutions for enhancing brain drug delivery. By mimicking natural cell properties, these systems have the potential to bypass BBB limitations, improve drug delivery efficiency, and overcome the barrier's selective permeability[11]. Biomimetic materials, disguised as biological substances, retain structural and functional properties while evading phagocytic clearance[12,13]. They offer advantages such as BBB penetration, biocompatibility, and tumor targeting[14]. In prior work[15], our research group encapsulated the tumor metabolism regulator Lonidamine and the photosensitizer Chlorin e6 (Ce6) into the core of zeolitic imidazolate framework-8 (ZIF-8) nanoparticles (NPs). The tumor cell membrane was subsequently coated onto the NP surface *via* membrane extrusion, creating biomimetic nanomaterials. Results showed that the CM coating formed biomimetic nanomaterials with cell-like behaviors, enabling them to "disguise" as endogenous substances. This reduced non-specific protein adsorption, prolonged circulation time in the body, and facilitated targeted delivery to tumor sites.

While cell membrane-coated biomimetic nanotechnology offers great potential for crossing the BBB, several challenges remain in achieving efficient anti-GBM efficacy. After injection, plasma proteins adsorb onto the NP surface, forming a protein corona (PC) that can alter NP properties, impair BBB penetration, and reduce drug accumulation in gliomas. Most studies focus on inert PCs that inhibit NP function, causing off-target effects or loss of efficacy[16,17]. However, some functional plasma proteins with intrinsic targeting abilities can adsorb onto NP surfaces, serving as endogenous targeting ligands[18,19]. A PC-mediated targeting strategy has been proposed to leverage absorbable proteins with active ligand properties to enhance NP functionality *in vivo*[20]. Surface engineering of NPs and *in situ* regulation of PC formation can promote the adsorption of specific functional plasma proteins, transporting NPs to target sites for active targeting[21], and were thus used in this study. Compared with exogenous substances, endogenous proteins elicit much lower immune and inflammatory responses[22]. Advances in nanotechnology have produced a wide range of NPs capable of crossing or bypassing the BBB for effective glioma treatment[3]. For instance, surface modification with BBB- or glioma-targeting peptides enables NPs to cross the BBB and specifically target tumor cells[23-25]. Transferrin (Tf), a protein found in high concentrations in blood, and its receptor (transferrin receptor, TfR), a transmembrane protein highly expressed in most tumor cells, present a promising PC-mediated targeting mechanism for NPs. We propose using the spontaneous formation of Tf-PC in blood circulation as an active targeting ligand to TfR-overexpressing brain tumor cells, improving BBB penetration and active targeting.

Photodynamic therapy (PDT) is a reactive oxygen species (ROS)-based anti-tumor strategy that activates photosensitizers (PS) through irradiation, transferring their excited-state energy to surrounding oxygen to generate ROS. This process enhances oxidative stress in cancer cells, ultimately leading to their destruction[26,27]. PDT is widely used in current anti-tumor research[28]. By irradiating the tumor site with a laser of a specific wavelength, ROS can be produced by the locally aggregated PSs, causing cell death, which improves safety and reduces systemic toxicity compared with traditional chemotherapy[29]. By directly killing tumor cells, PDT activates the host anti-tumor immune response and induces immunogenic cell death (ICD), a process referred to as photodynamic immunotherapy (PDIT)[30,31]. Photosensitizers activated by localized laser irradiation induce PDT, selectively damaging tumor tissue while sparing normal tissue. However, the hypoxic microenvironment of solid tumors presents a major limitation for PDT[26], as insufficient oxygen availability significantly reduces its efficacy[32]. Addressing tumor hypoxia is thus crucial for enhancing PDT outcomes. Metformin (MET), an effective respiratory inhibitor, offers a solution to this issue. By inhibiting complex I in the mitochondrial respiratory chain, MET reduces the rate of oxygen consumption, thereby reversing tumor hypoxia and improving the therapeutic efficacy of PDT[33]. This provides a novel strategy for addressing the hypoxic tumor microenvironment and optimizing PDT.

Building on this foundation, we designed a nanodelivery platform incorporating an endogenous Tf- and homologous dual-targeting system (Fig. 1). First, the photosensitizer Ce6 and hypoxic inhibitor MET were co-loaded into liposomes. Next, U87 glioblastoma cell membranes were extracted and coated onto the liposome surface to create biomimetic nanomaterials with cell-like properties. These materials effectively "disguise" themselves as endogenous substances, reducing nonspecific protein adsorption, extending systemic circulation, and specifically targeting diseased tissues. Finally, the T_{10} peptide (sequence: CGGGHKYLRW),

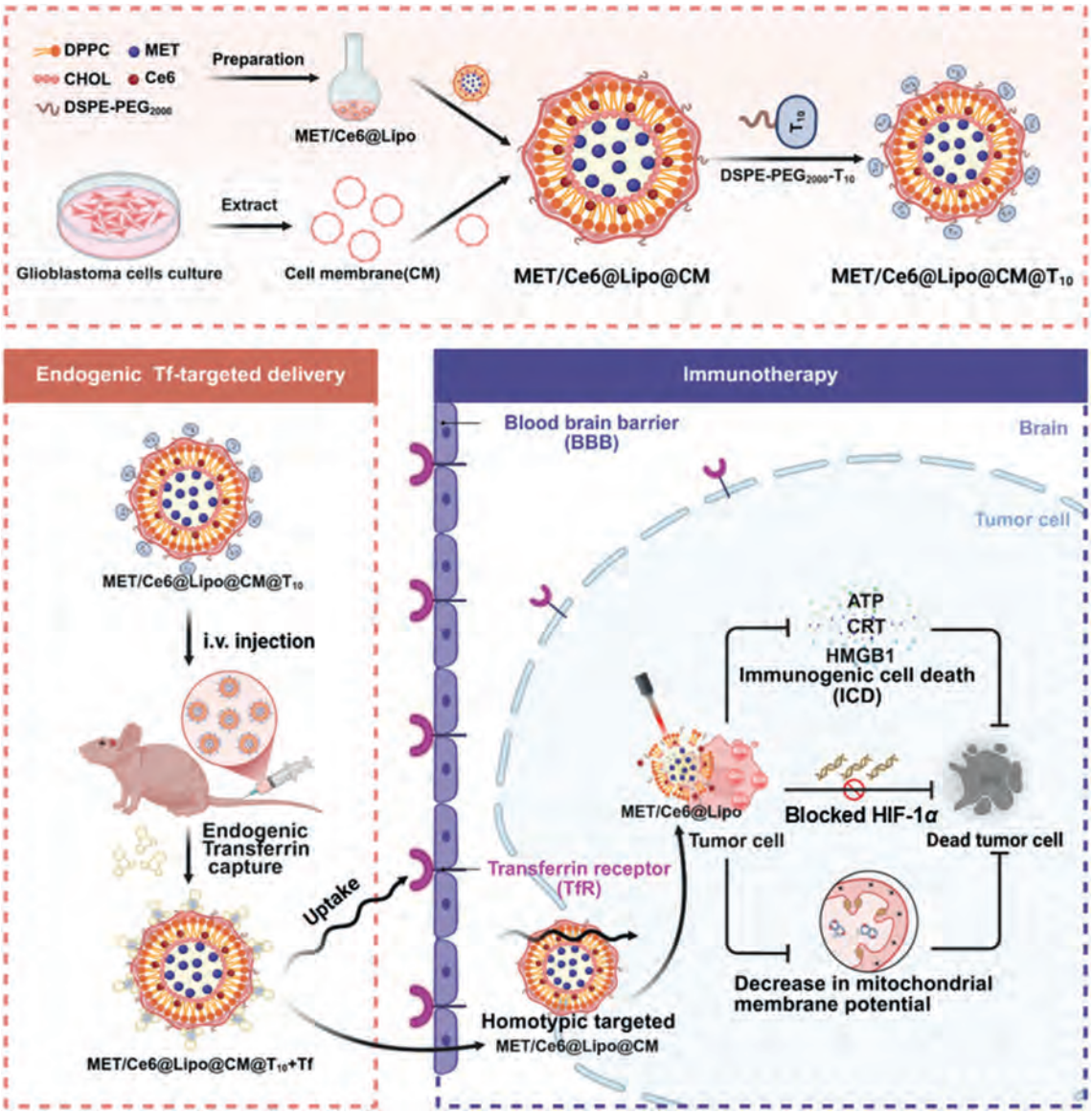

Figure 1 Schematic illustration of design and preparation of the MET/Ce6@Lipo@CM@T_{10} and enhanced photodynamic therapy of glioblastoma under dual-targeting by transferrin corona and cell membrane.

which exhibits a high affinity for Tf in blood, was modified on the surface of the membrane-coated liposomes. This enabled the preparation of a lipo-complex with BBB-crossing and endogenous active-targeting capabilities. The aim of this study was to develop a rational platform for combining PDT with immunoadjuvant therapy to enhance PDT-induced immune responses and improve ROS production efficiency. Simultaneously, the delivery system leverages the PC effect and homologous cell-homing properties to efficiently deliver drugs to the brain, addressing lesions and offering a new approach to glioblastoma treatment.

2. Materials and methods

2.1. Synthesis and structural characterization of DSPE-PEG_{2000}-T_{10}

The 1,2-distearoyl-*sn*-glycero-3-phosphoethanolamine-*N*-[methoxy (polyethylene glycol)2000]-T_{10} (DSPE-PEG_{2000}-T_{10}) copolymer was synthesized by coupling the N-terminal cysteine-attached T_{10} peptide to the terminal Mal group of DSPE-PEG_{2000}-MAL *via* a Michael addition reaction. Specifically, a suspension was prepared by mixing DSPE-PEG_{2000}-MAL (29.0 mg, 0.1 mmol) with an aqueous solution of the T_{10} peptide (12.2 mg, 0.12 mmol). Then, 10 mL of HEPES buffer (0.1 mol/L, pH 8.0) was added to the suspension, which was stirred at room temperature for 24 h using a magnetic stirrer. Unreacted T_{10} peptide was removed by dialysis against distilled water (MWCO 2.5 kDa) for 24 h. The purified DSPE-PEG_{2000}-T_{10} was obtained *via* freeze-drying, and its structure was confirmed through ^{1}H NMR spectroscopy (600 MHz) and MALDI-TOF MS.

2.2. Preparation of MET/Ce6@Lipo

A mixture of 8 mg DPPC, 4 mg cholesterol, 3 mg DSPE-PEG_{2000}, and 1 mg Ce6 was dissolved in 2 mL chloroform and 2 mL methanol. After ultrasonic dissolution, the organic solvent was

removed by rotary evaporation for 30 min in a 45 °C water bath, forming a uniform lipid-drug film on the container wall. The film was hydrated with MET solution (4 mg MET dissolved in 1 mL PBS) under a 45 °C water bath for 60 min, followed by sonication for 10 min (power: 60 W, 2-s intervals). The resulting product was MET/Ce6@Lipo.

2.3. Preparation of U87 cell membrane (CM) vesicles

U87 cell membrane vesicles were prepared using the extrusion method[34]. U87 cells were resuspended in membrane protein extraction buffer (with PMSF) and centrifuged at 4 °C and 700×*g* for 10 min. The precipitate was washed, centrifuged, and freeze-dried to obtain tumor cell membrane fragments. A portion of the dry membrane powder was dissolved in ddH_2O, subjected to 10 min of ultrasonication, and extruded through a 400 nm polycarbonate membrane using a liposome extruder for 10 cycles, yielding U87 cell membrane vesicles.

2.4. Preparation of MET/Ce6@Lipo@CM

Equal volumes (1:1) of prepared CM vesicles and MET/Ce6@Lipo were mixed. The mixture was extruded through a 400 nm polycarbonate membrane for 10 cycles using a liposome extruder, followed by centrifugation at 9279×*g* for 20 min to remove unbound vesicles and liposomes. The resultant MET/Ce6@Lipo@CM was washed with PBS.

2.5. Preparation of MET/Ce6@Lipo@CM@T_{10}

DSPE-PEG_{2000}-T_{10} and MET/Ce6@Lipo@CM were gently stirred in the dark at 4 °C for 6 h at a mass ratio of 2:1 (DSPE-PEG_{2000}-T_{10} to CM). The mixture was then ultracentrifuged to obtain MET/Ce6@Lipo@CM@T_{10}. To mimic the formation of Tf-PC *in vivo*, MET/Ce6@Lipo@CM@T_{10} was incubated with a 10 mg/mL Tf solution for 1 h, followed by two rounds of ultrafiltration using ultrafiltration centrifugal tubes (MWCO 100 kD, 13,362×*g*, 1 h, 4 °C). The final product, MET/Ce6@Lipo@CM@T_{10}+Tf, was resuspended in PBS (pH 7.4).

2.6. Characterization of MET/Ce6@Lipo@CM@T_{10}

The particle size distribution, PDI, and Zeta potential of the lipocomplexes were measured using a Malvern particle size analyzer after dilution with PBS to the appropriate concentration. Morphological observations were conducted using transmission electron microscopy (TEM). Storage stability was evaluated at 4 °C over 7 days by measuring changes in particle size and PDI. The ultraviolet absorption of different formulations was determined using UV−Vis spectroscopy at detection wavelengths of 236 (MET) and 401 nm (Ce6). The encapsulation efficiency (EE %) of MET/Ce6@Lipo@CM@T_{10} was calculated according to Eq. (1):

$$\mathrm{EE}\,(\%) = \left(W_{\text{drug in lipo}} \,/\, W_{\text{total drug}}\right) \times 100 \quad (1)$$

To determine the drug loading of Ce6 and MET in final preparation, after freeze-drying MET/Ce6@Lipo@CM@T_{10}, 2 mg of the product was weighed and dissolved in methanol. According to the above detection conditions, the content of Ce6 and MET was measured separately, and the drug loading was calculated according to Eq. (2):

$$\mathrm{DL}\,(\%) = \left(W_{\text{drug in lipo}} \,/\, W_{\text{lipo}}\right) \times 100 \quad (2)$$

2.7. In vitro drug release study

The release profile of MET/Ce6@Lipo@CM@T_{10} was investigated using the dialysis method. A 1 mL solution of MET/Ce6@Lipo@CM@T_{10} (containing Ce6 at 0.625 μg/mL and MET at 2.5 μg/mL) was transferred into a dialysis bag (MWCO 10 kDa) and immersed in 20 mL of PBS (pH 7.4, containing 0.5% Tween-80). The solution was shaken at 37 °C at a rotational speed of 100 rpm (SW 23, Julabo, Seelbach, Germany). At predetermined time points, 0.5 mL samples were collected, and an equal volume of fresh medium preheated to 37 °C was added. The collected samples were centrifuged at 13,362×*g* for 10 min, and the supernatant was analyzed to determine the concentrations of Ce6 and MET using a UV spectrophotometer.

2.8. SDS-PAGE protein analysis

The immune escape and homologous targeting ability of MET/Ce6@Lipo@CM@T_{10} are primarily attributed to the membrane proteins present on the CM. The retention of these membrane proteins in U87 tumor cells was analyzed using SDS-PAGE electrophoresis. Standard solutions of varying concentrations of samples were placed in 96-well plates, incubated at 37 °C for 30 min, and the absorbance (OD) at 562 nm was measured using an enzymometer. Each sample was tested in quadruplicate, and standard curves were drawn to calculate the protein content and loading amount. The retention of protein bands was observed following the SDS-PAGE gel reagent instructions.

2.9. Study of PC formation ability

To evaluate whether NPs modified with the T_{10} peptide bind Tf and form a PC *in vivo*, Tf content was analyzed. BALB/c mice were anesthetized with isoflurane, and blank liposomes (Lipo) and T_{10}-modified blank liposomes (Lipo@T_{10}) were injected intravenously *via* the tail vein at a lipid dose of 0.125 mmol/L/g body weight[35]. Liposomes were recovered from 0.5 mL blood samples collected 10 min post-injection. Plasma was prepared by mixing with EDTA through gentle inversion of the collection tubes, followed by centrifugation at 835×*g* for 10 min at 4 °C. Plasma samples from three mice were further centrifuged at 13,362×*g* for 1 h at 4 °C, and the pellet was washed three times with cold PBS to isolate *in vivo* PC liposomes. These PC liposomes were purified using Sepharose CL-4B column chromatography, concentrated by ultrafiltration, and analyzed *via* Western blotting.

To identify the specific protein components forming the PC *in vivo*, mice were injected with MET/Ce6@Lipo, MET/Ce6@Lipo@CM, and MET/Ce6@Lipo@CM@T_{10} through the tail vein. Samples from each group were recovered and analyzed by LC−MS. In addition, to study the impact of the cell membrane's protein composition on *in vivo* protein corona formation, we analyzed CM and MET/Ce6@Lipo@CM@T_{10} for their protein compositions. The protein database was searched using MaxQuant (v. 1.6.2.10) to identify proteins from the mass spectrometry data.

2.10. Cell culture

U87 cells were cultured in Dulbecco's modified Eagle's medium (DMEM) medium supplemented with 10% FBS and 1%

streptomycin−penicillin. Similarly, brain-derived Endothelial cell.3 (bEnd.3) cells were cultured in DMEM with 10% FBS and 1% streptomycin−penicillin. Both cell types were incubated at 37 °C in a 5% CO_2 atmosphere. Cells in the logarithmic growth phase were used for subsequent experiments.

2.11. Cell uptake assay

The cellular uptake of Ce6@Lipo@CM@T_{10} by U87 cells was analyzed using confocal laser scanning microscopy (CLSM) and flow cytometry. U87 cell membranes were labeled with DiO dye solution, incubated at 37 °C for 30 min, washed with PBS, and centrifuged to obtain DiO-labeled U87 cell membranes (DiO@CM).

U87 cells in the logarithmic growth phase were seeded into 12-well plates at a density of 3.0×10^5 cells per well and cultured for 24 h Ce6@Lipo, DiO@CM, Ce6@Lipo/DiO@CM, and Ce6@Lipo/DiO@CM@T_{10} were diluted (Ce6 concentration: 0.625 μg/mL) and added to the corresponding wells for a 4-h incubation. After incubation, cells were washed three times with PBS, fixed with 4% paraformaldehyde, and stained with 4′,6-diamidino-2-phenylindole (DAPI). CLSM was used to observe NP uptake in U87 cells.

In a parallel experiment, U87 cells were seeded at a density of 1.5×10^5 cells per well, incubated for 24 h, and treated with Ce6@Lipo, Ce6@Lipo@CM, Ce6@Lipo@CM@T_{10}, or Ce6@Lipo@CM@T_{10}+Tf (Ce6 concentration: 0.625 μg/mL). Serum-free DMEM served as a blank control. Cells were incubated for 4 h, centrifuged, resuspended in PBS, and analyzed by flow cytometry to determine uptake efficiency.

2.12. ROS/ID activity

Functional tests of hypoxia and oxidative stress levels in living cells were performed using fluorescence microscopy to determine ROS/ID activity. The ROS-sensitive fluorescent probe DCFH-DA (2′,7′-dichlorofluo-esceindiacetate) and Hypoxiaprobe-1 were used for these analyses. U87 cells in the logarithmic growth phase were seeded into 12-well plates at a density of 5.0×10^4 cells per well and cultured at 37 °C with 5% CO_2 for 24 h, and MET@Lipo, Ce6@Lipo, MET/Ce6@Lipo, MET/Ce6@Lipo@CM, MET/Ce6@Lipo@CM@T_{10}, and MET/Ce6@Lipo@CM@T_{10}+Tf (Ce6 concentration: 0.625 μg/mL) were added to the respective wells. For the irradiation group, cells were exposed to 640 nm laser irradiation for 5 min. Cells were washed three times with PBS, treated with fluorescent probes (DCFH-DA at 1:1000 and Hypoxiaprobe-Red in serum-free DMEM medium at 1:2000), and observed under an inverted fluorescence microscope.

2.13. Expression of HIF-1α in cells treated with MET/Ce6@Lipo@CM@T_{10}

U87 cells in the logarithmic growth phase were seeded into 6-well plates at a density of 3.0×10^5 cells per well and incubated for 24 h. The cells were treated with MET@Lipo, Ce6@Lipo, MET/Ce6@Lipo, MET/Ce6@Lipo@CM, MET/Ce6@Lipo@CM@T_{10}, or MET/Ce6@Lipo@CM@T_{10}+Tf (Ce6 concentration: 0.625 μg/mL, MET concentration: 2.5 μg/mL) for 4 h. Cells in the irradiation group were exposed to 640 nm laser irradiation for 5 min, followed by 20 h of incubation. Cells were collected, and the expression of HIF-1α was measured by Western blot analysis.

2.14. Hypoxia-alleviation ability of MET/Ce6@Lipo@CM@T_{10}

To study the effect of MET on mitochondrial complex I, Mitochondrial Respiratory Complex I Activity Assay Kit (Boxbio, Beijing, China) was used for measurement. In short, U87 cells in the logarithmic growth phase were seeded into 100 mm dishes to about 5×10^6 per dish. Cells were treated with MET@Lipo, Ce6@Lipo, MET/Ce6@Lipo, MET/Ce6@Lipo@CM, MET/Ce6@Lipo@CM@T_{10}, or MET/Ce6@Lipo@CM@T_{10}+Tf (Ce6 concentration: 0.625 μg/mL, MET concentration: 2.5 μg/mL) for 4 h, and were exposed to 640 nm laser irradiation for 5 min. The sample was homogenized in an ice bath and centrifuged at 11,000×g for 15 min. The pellet was then sonicated to prepare it for subsequent use. The activity of Mitochondrial Respiratory Complex I Activity was measured using a spectrophotometer. The absorbance at 340 nm was recorded at $t = 10$ s (A_1) and at $t = 70$ s (A_2). The activity was calculated according to Eq. (3):

$$\text{Activity (U / mg protein)} = (3215.43 \times (A_1 - A_2) / \text{Cpr}) \quad (3)$$

where Cpr is the sample protein concentration (mg/mL).

U87 cells in the logarithmic growth phase were seeded into a Corning 96-well black polystyrene microplate at a density of 1.0×10^4 cells per well and incubated for 24 h. Cells were treated with MET@Lipo, Ce6@Lipo, MET/Ce6@Lipo, MET/Ce6@Lipo@CM, MET/Ce6@Lipo@CM@T_{10}, or MET/Ce6@Lipo@CM@T_{10}+Tf (Ce6 concentration: 0.625 μg/mL, MET concentration: 2.5 μg/mL) for 4 h, and were exposed to 640 nm laser irradiation for 5 min. According to the steps in the manual of the OCR detection kit (Elabscience, Wuhan, China), place the microplate in a multi-functional microplate reader at 37 °C and adopt the dynamic reading mode. The fluorescence value is plotted over time, and the OCR is represented by the slope of the curve.

2.15. Mitochondrial membrane potential analyses

To determine whether MET/Ce6@Lipo@CM@T_{10} can induce mitochondrial damage in tumor cells under irradiation, changes in mitochondrial membrane potential ($\Delta\Psi m$) were detected using the JC-1 fluorescence probe. U87 cells in the logarithmic growth phase were seeded into 12-well plates at a density of 3.0×10^5 cells per well and incubated for 24 h. The cells were treated with MET@Lipo, Ce6@Lipo, MET/Ce6@Lipo, MET/Ce6@Lipo@CM, MET/Ce6@Lipo@CM@T_{10}, or MET/Ce6@Lipo@CM@T_{10}+Tf (Ce6 concentration: 0.625 μg/mL, MET concentration: 2.5 μg/mL) for 4 h. Cells in the irradiation group were exposed to 640 nm laser irradiation for 5 min, followed by 20 h of incubation. After washing with PBS, JC-1 staining solution was added and incubated at 37 °C for 20 min. Changes in mitochondrial membrane potential were observed using CLSM.

2.16. Investigation of ICD-related signaling factors

U87 cells in the logarithmic growth phase were seeded into 12-well plates at a density of 5.0×10^4 cells/well and cultured for 24 h. After incubation, MET@Lipo, Ce6@Lipo, MET/Ce6@Lipo, MET/Ce6@Lipo@CM, MET/Ce6@Lipo@CM@T_{10}, and MET/Ce6@Lipo@CM@T_{10}+Tf (with Ce6 at 0.625 μg/mL and MET at 2.5 μg/mL) were added to the corresponding wells and incubated for 4 h. U87 cells in the irradiation group were exposed to laser irradiation at a wavelength of 640 nm

for 5 min, followed by incubation for 20 h. After incubation, the cells were washed three times with PBS, fixed with 4% paraformaldehyde for 15 min, and permeabilized with 0.1% Triton X-100 for 10 min. CRT (1:1000) and HMGB1 (1:400) primary antibodies were added and incubated at 37 °C for 2 h, followed by a 1-h incubation with Alexa Fluor 488-conjugated secondary antibodies. The cells were then observed using CLSM.

U87 cells in the logarithmic growth phase were seeded into 6-well plates at a density of 3.0×10^5 cells/well and cultured for 24 h. The treatment groups, doses, laser wavelength, and irradiation times used were the same as those described for the CRT and HMGB1 analysis. After incubation, 200 μL of ATP lysis buffer was added to each well, and the samples were centrifuged at 4 °C and 12,000×*g* for 5 min. The supernatant was collected and analyzed using an ATP ELISA kit according to the manufacturer's instructions to measure ATP release.

2.17. Cytotoxicity study

The cytotoxicity of the blank carrier material and the inhibitory effect of MET/Ce6@Lipo@CM@T_{10} on U87 cells were assessed using a CCK-8 assay. U87 cells in the logarithmic growth phase were seeded into 96-well plates at a density of 5×10^3 cells/well and cultured for 24 h. Blank Lipo, Blank Lipo@CM, and Blank Lipo@CM@T_{10} were diluted to concentrations of 3.125, 6.25, 12.5, 25.0, and 50.0 μg/mL and added to the respective wells. After 24 or 48 h of culture, 10% CCK-8 reagent was added to each well, and the OD at 450 nm was measured.

For further evaluation, U87 (TfR over-expression), Caco-2 (TfR low-expression), and bEnd.3 (TfR low-expression) cells were seeded into 96-well plates at the same density and cultured for 24 h Ce6@Lipo, MET/Ce6@Lipo, MET/Ce6@Lipo@CM, MET/Ce6@Lipo@CM@T_{10}, and MET/Ce6@Lipo@CM@T_{10}+Tf (with Ce6 at 0.625 μg/mL) were added to the wells and incubated for 4 h. Cells in the irradiation group were exposed to a 640 nm laser for 5 min, then cultured for either 20 or 44 h. OD values were measured after CCK-8 treatment. The unilluminated group omitted the laser step.

2.18. Cell apoptosis

U87 cells in the logarithmic growth phase were seeded into 12-well plates at a density of 1.5×10^5 cells/well and cultured for 24 h. MET@Lipo, Ce6@Lipo, MET/Ce6@Lipo, MET/Ce6@Lipo@CM, MET/Ce6@Lipo@CM@T_{10}, and MET/Ce6@Lipo@CM@T_{10}+Tf (with Ce6 at 0.625 μg/mL and MET at 2.5 μg/mL) were diluted and added to the corresponding wells, followed by a 4-h incubation. Cells in the light group were exposed to laser irradiation at 640 nm for 5 min and then cultured for 20 h. Afterward, the cells were digested with 0.25% trypsin without EDTA, and the cell suspensions were collected. The cells were treated with Annexin V-FITC and PI staining solutions, and apoptosis was analyzed using flow cytometry.

2.19. Calcein-AM live cell staining

U87 cells in the logarithmic growth phase were seeded into 12-well plates at a density of 3.0×10^5 cells/well and cultured for 24 h. MET@Lipo, Ce6@Lipo, MET/Ce6@Lipo, MET/Ce6@Lipo@CM, MET/Ce6@Lipo@CM@T_{10}, and MET/Ce6@Lipo@CM@T_{10}+Tf (with Ce6 at 0.625 μg/mL and MET at 2.5 μg/mL) were diluted and added to the corresponding wells, followed by a 4-h incubation. Cells in the irradiation group were exposed to a 640 nm laser for 5 min, then cultured for 20 h. Afterward, the cells were washed with PBS, and 500 μL of diluted Calcein-AM working solution was added to each well. The cells were incubated at 37 °C in the dark for 30 min and then observed using an inverted fluorescence microscope.

2.20. In vitro BBB transcytosis study

To assess the BBB penetration efficiency of the lipo-complexes, bEnd.3 cells in the logarithmic growth phase were seeded into the upper chamber of a 12-well Transwell plate at a density of 1×10^5 cells/well. The lower chamber was filled with 1.5 mL of DMEM containing 10% FBS, and the plates were incubated at 37 °C with 5% CO_2. The medium was changed every two days, and *trans*-epithelial electrical resistance (TEER) was measured[36]. A TEER value of 200 $\omega.cm^2$ indicated the formation of a dense, confluent monolayer with tight junctions. When the TEER value reached 200 $\omega.cm^2$, U87 cells were seeded into the lower chamber at a density of 1×10^5 cells/well and cultured for 24 h. Free Ce6, Ce6@Lipo, Ce6@Lipo@CM, Ce6@Lipo@CM@T_{10}, and Ce6@Lipo@CM@T_{10}+Tf (with Ce6 at 0.625 μg/mL and MET at 2.5 μg/mL) were added to the upper chamber with serum-free DMEM and incubated for 4 h. Cells in the light group were exposed to a 640 nm laser for 5 min and then cultured for 2 h, while cells in the unilluminated group were cultured for 2 h without irradiation. The cross-BBB uptake of the lipo-complexes was observed using CLSM.

2.21. Permeability of MET/Ce6@Lipo@CM@ T_{10} into 3D tumor spheres in vitro

A 3D tumor sphere model was established using U87 cells to evaluate the tissue permeability of the lipo-complexes. U87 cells in the logarithmic growth phase were seeded onto 2% agarose-coated plates at a density of 2.0×10^3 cells/well. When the diameter of the tumor sphere reaches about 300 μm, tumor sphere were divided into six groups, Free Ce6, MET/Ce6@Lipo, MET/Ce6@Lipo@CM, MET/Ce6@Lipo@CM@T_{10}, MET/Ce6@Lipo@CM@T_{10}+Tf or MET/Ce6@Lipo@CM@T_{10}+Tf (L+). After incubated for 4 h, MET/Ce6@Lipo@CM@T_{10}+Tf (L+) group was exposed to laser irradiation at 640 nm for 5 min, followed by 2 h of culture. Cells in the unilluminated group were cultured for 2 h without laser exposure. After incubation, tumor spheres were collected using a 1 mL pipette, washed three times with PBS, and scanned with CLSM at 10 μm intervals from the top to the middle plane to assess lipo-complex penetration.

2.22. Animals and tumor models

All animal experiments were approved by the Laboratory Animal Ethics Committee of the Institute of Pharmaceutical Sciences, Chinese Academy of Medical Sciences, and Peking Union Medical College (Approval No. 00004427). U87-Luc cells were digested with 0.25% pancreatic enzyme, centrifuged, washed twice with PBS, and re-suspended in PBS at a density of 7.5×10^4 cells/μL. The cell suspension was kept on ice for later use. Male BALB/c nude mice (4−6 weeks old, weighing 16−18 g) were anesthetized using 2% isoflurane inhalation. The mice were secured onto a brain stereoscope, and the head skin was disinfected with alcohol before being incised with surgical scissors. Hydrogen peroxide (5%) was applied using a medical cotton

swab. A drill hole was made 1.8 mm lateral to the pre-bregma (near the striatum), and 4 μL of the U87-Luc cell suspension was injected at a constant rate of 1 μL/min. After the injection, the needle was left in place for 5 min before being slowly withdrawn. The drill hole was sealed with bone wax, and the scalp incision was sterilized and sutured. After surgery, the mice were placed under an infrared therapy apparatus for recovery and later returned to their cages. All procedures were performed on a clean bench to minimize the risk of surgical site infection.

2.23. *In vivo distribution and brain targeting analyses*

Nude mice with orthotopic brain gliomas were randomly divided into four groups seven days after tumor implantation. Each group received a 200 μL tail vein injection of free Ce6, Ce6@Lipo, Ce6@Lipo@CM, or Ce6@Lipo@CM@T_{10} (Ce6 concentration: 0.25 mg/mL). At 2, 4, 6, 8, and 24 h post-injection, the mice were anesthetized with isoflurane and imaged using a live animal imaging system to capture fluorescence signals. At the final time point, the mice were euthanized *via* cervical dislocation, and major organs (heart, liver, spleen, lungs, kidneys, and brain tissue) were harvested. Fluorescence signals were recorded using *in vitro* fluorescence imaging to assess the biodistribution. Quantitative fluorescence signal analysis was performed using Living Image software.

To further investigate the tumor cell membrane-mediated homologous targeting and the T_{10}-mediated active targeting of the lipo-complexes, brain tissue frozen sections were analyzed for BBB penetration and glioma distribution. Orthotopic glioma-bearing nude mice were treated as described above. Three hours after injection, the mice were anesthetized and euthanized *via* cervical dislocation. Brains were harvested, sectioned into 10-μm slices, stained with DAPI, and analyzed using CLSM to observe fluorescence distribution in the tumor.

2.24. *In vivo anti-tumor efficacy*

Ten days after establishing the orthotopic glioblastoma model, the mice were randomly divided into seven groups ($n = 3$): PBS, PBS(L+), MET@Lipo(L+), Ce6@Lipo(L+), MET/Ce6@Lipo(L+), MET/Ce6@Lipo@CM(L+), and MET/Ce6@Lipo@CM@T_{10}(L+). Each formulation was administered *via* tail vein at a volume of 200 μL per animal. Ce6 and MET doses were 2.5 and 10.0 mg/kg, respectively, and were given every three days for a total of five doses. Four hours after each injection, laser irradiation (640 nm, 0.8 W/cm^2) was applied to the skull tumor site for 5 min. The laser's power, duration, and probe distance were maintained consistently across all mice. Brain tumor fluorescence signals were monitored using live animal imaging on Days 10, 17, and 24 post-treatment to assess glioma growth. At the study's conclusion, the mice were euthanized *via* cervical dislocation, and brain tissues were harvested, embedded, and sectioned for hematoxylin-eosin (H&E) staining. Tumor tissue apoptosis and HIF-1α expression were analyzed using TUNEL and immunofluorescence staining.

2.25. *In vivo safety*

During the treatment period, changes in body weight were recorded. After the final dose, blood samples were collected to measure serum levels of aspartate aminotransferase (AST), alanine aminotransferase (ALT), blood urea nitrogen (BUN), and creatinine (CRE). Major organs (heart, liver, spleen, lungs, and kidneys) were fixed in neutral formalin, embedded in paraffin, and subjected to H&E staining for histopathological evaluation.

2.26. *Statistical analyses*

All data are expressed as mean ± standard deviation (SD) and analyzed with GraphPad Prism 9.5. Differences between groups were compared *via* one-way ANOVAs or Student's *t*-test. $*P < 0.05$, $**P < 0.01$, $***P < 0.001$.

3. Results and discussion

3.1. *Structural characterization of DSPE-PEG$_{2000}$-T$_{10}$*

DSPE-PEG_{2000}-T_{10} was synthesized *via* a reaction between the MAL group of DSPE-PEG_{2000}-Mal and the SH group of the T_{10} peptide. As shown in Supporting Information Fig. S1, the characteristic MAL peak at $\delta = 6.74$ ppm disappeared in the ^{1}H NMR spectrum of DSPE-PEG_{2000}-T_{10}. The MALDI-TOF-MS results, presented in Supporting Information Fig. S2, indicated that the main peaks of DSPE-PEG_{2000}-Mal were at 2099 and 2974, while the molecular weight range shifted to 4002−2970 after synthesis with T_{10}. The T_{10} peptide had a molecular weight of approximately 1010, consistent with the additional molecular weight observed. These results, together with ^{1}H NMR analysis, confirmed the successful conjugation of T_{10} to DSPE-PEG_{2000}.

3.2. *Preparation and characterization of MET/Ce6@Lipo@CM@T$_{10}$*

The preparation scheme for the lipo-complex is illustrated in Fig. 2A. Initially, MET and Ce6 were encapsulated in liposomes (MET/Ce6@Lipo). Next, U87 cell membranes were extracted and coated onto the liposomes to form membrane-coated liposomes (MET/Ce6@Lipo@CM). Finally, DSPE-PEG_{2000}-T_{10} copolymer was incorporated into MET/Ce6@Lipo@CM, resulting in the final lipo-complex (MET/Ce6@Lipo@CM@T_{10}).

Fig. 2B and C shows the particle size distributions of CM, Blank Lipo, MET/Ce6@Lipo, MET/Ce6@Lipo@CM, and MET/Ce6@Lipo@CM@T_{10}, all of which exhibited unimodal and uniform distributions. The particle sizes of MET/Ce6@Lipo, MET/Ce6@Lipo@CM, and MET/Ce6@Lipo@CM@T_{10} were 97.80 ± 2.43, 101.2 ± 2.30, and 108.9 ± 2.90 nm, respectively, with PDIs of 0.186 ± 0.05, 0.229 ± 0.04, and 0.263 ± 0.03. Their zeta potentials were -35.6 ± 1.80, -34.4 ± 2.02, and -30.0 ± 1.95 mV, respectively. The increase in particle size and gradual reduction in zeta potential after membrane coating and T_{10} modification confirmed the successful synthesis of the drug-loaded, membrane-coated, and T_{10}-modified NPs. The NPs, with sizes between 50 and 200 nm, have been reported to exhibit enhanced tumor tissue accumulation *via* the Enhanced Permeability and Retention (EPR) effect[37]. TEM analysis of the NPs, presented in Fig. 2D, revealed distinct morphologies. CM displayed a spherical vesicle structure, while Blank Lipo and MET/Ce6@Lipo exhibited smooth, double-layer spherical structures. MET/Ce6@Lipo@CM, coated with U87 tumor cell membranes, exhibited a prominent core−shell structure. Further modification with T_{10} produced MET/Ce6@Lipo@CM@T_{10}, which retained the core−shell morphology with increased size, consistent with particle size measurements.

UV spectrophotometry was used to detect the characteristic absorption peaks of each preparation (Fig. 2E). No significant absorption peak was observed in the Blank Lipo group. In the

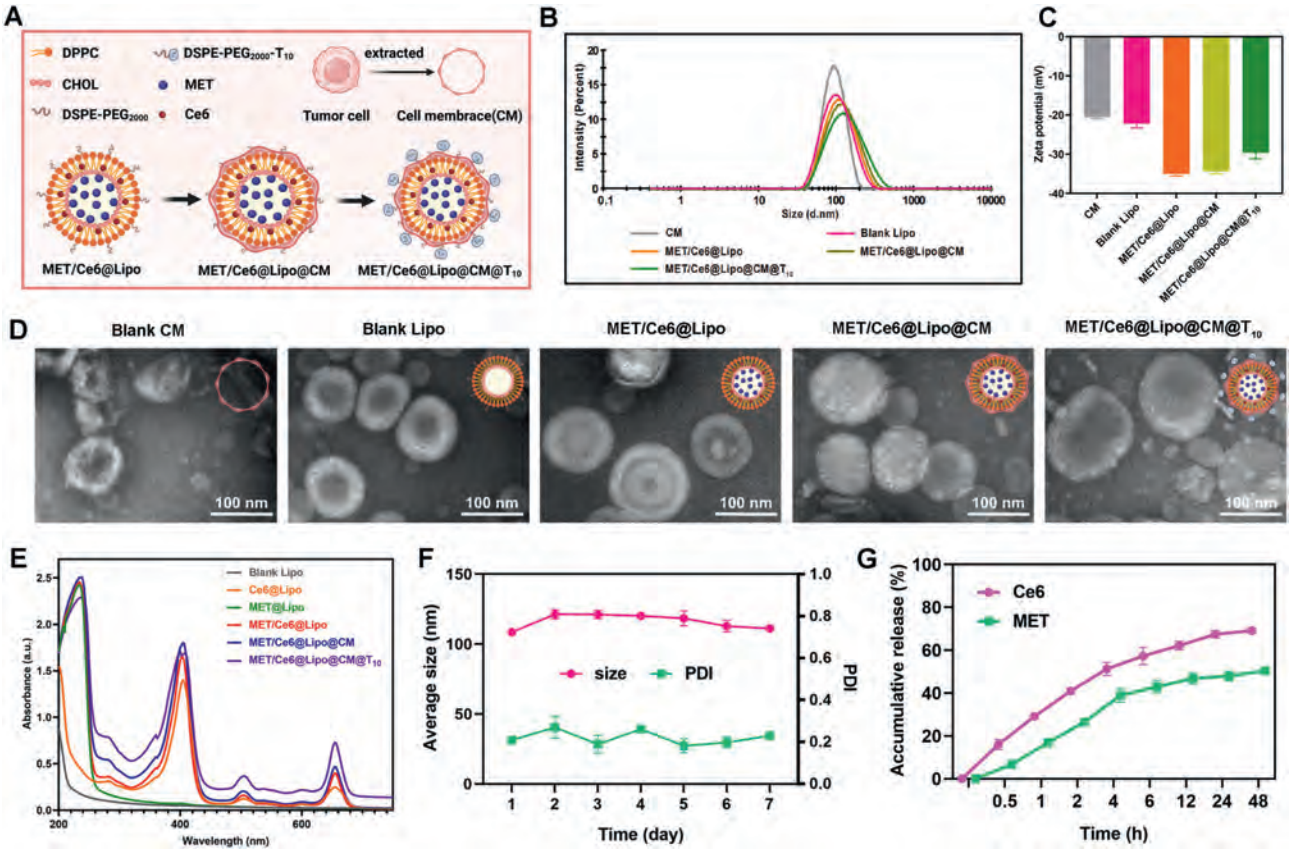

Figure 2 Preparation and characterization of MET/Ce6@Lipo@CM@T_{10}. (A) Schematic diagram of the MET/Ce6@Lipo@CM@T_{10} preparation. (B) Particle sizes of different formulations. (C) Zeta potentials of different formulations. (D) TEM images of different formulations. (E) UV−vis absorption spectra. (F) Storage stability of MET/Ce6@Lipo@CM@T_{10}. (G) *In vitro* release of Ce6 and MET in MET/Ce6@Lipo@CM@T_{10}. $n = 3$.

mono-drug-loaded groups, Ce6@Lipo displayed characteristic absorption peaks at 404 and 660 nm, while the MET@Lipo group showed a peak at 232 nm, consistent with literature reports. The MET/Ce6@Lipo, MET/Ce6@Lipo@CM, and MET/Ce6@Lipo@CM@T_{10} groups exhibited distinct absorption peaks at 232, 404, and 660 nm, confirming the successful encapsulation of Ce6 and MET into the liposomes. In addition, the UV absorption peaks of the drugs remained intact after lipid encapsulation, membrane coating, and T_{10} targeting modification, indicating that the carrier material did not interfere with drug absorption. The EE and DL of Ce6 in MET/Ce6@Lipo@CM@T_{10} were 83.3% and 3.05%, while that of MET in MET/Ce6@Lipo@CM@T_{10} were 58.0% and 8.86%, respectively.

Storage stability is a crucial parameter in drug delivery systems. MET/Ce6@Lipo@CM@T_{10} was stored in PBS at 4 °C for seven days (Fig. 2F), during which it remained clear and transparent with no visible drug precipitation. Furthermore, particle size and PDI remained consistent over time, showing minimal changes. These results demonstrated that MET/Ce6@Lipo@CM@T_{10} possesses excellent stability, supporting its potential for subsequent *in vitro* and *in vivo* applications.

The *in vitro* drug release study of MET/Ce6@Lipo@CM@T_{10} revealed that the release rates of MET and Ce6 were 50.12% and 67.05% (Fig. 2G), respectively, within the first 24 h. The release rates gradually slowed over time, following a sustained-release profile without any burst release. After 48 h, the cumulative release rates for MET and Ce6 were 53.01% and 68.18%, respectively. These findings demonstrated that the synthesis method and structure of DSPE-PEG_{2000}-T_{10} were appropriate, as confirmed by its characterization. The preparation process of transferrin-corona-mediated cell membrane-coated biomimetic nanoparticles (MET/Ce6@Lipo@CM@T_{10}) was simple and resulted in favorable physicochemical properties. Using Ce6 as a photosensitizer, MET—a mitochondrial oxidative phosphorylation inhibitor—was incorporated into the liposomal system *via* the thin-film dispersion method. Water-soluble MET and lipid-soluble Ce6 were encapsulated within the aqueous core and lipid bilayer of the liposomes, respectively, with the outer layer covered by a cell membrane. This design facilitated sustained drug release without burst effects, providing a robust foundation for further *in vitro* efficacy studies and *in vivo* pharmacodynamic evaluations.

3.3. Evaluation of the Tf binding ability of T_{10} and PC characterization

Liposome−PC complexes (L−PCs) were recovered and isolated from the blood circulation in BALB/c mice (Fig. 3A). To evaluate the ability of T_{10} to bind Tf *in vivo*, we administered Blank Lipo and Blank Lipo@T_{10} *via* the tail vein of mice and subsequently recovered them. Tf levels on the liposome surfaces were then assessed using WB. As shown in Fig. 3B and C, Tf expression on the T_{10}-modified liposomes was significantly higher than on unmodified liposomes (***$P < 0.001$). These results demonstrated that T_{10}-modified liposomes exhibited excellent Tf binding ability

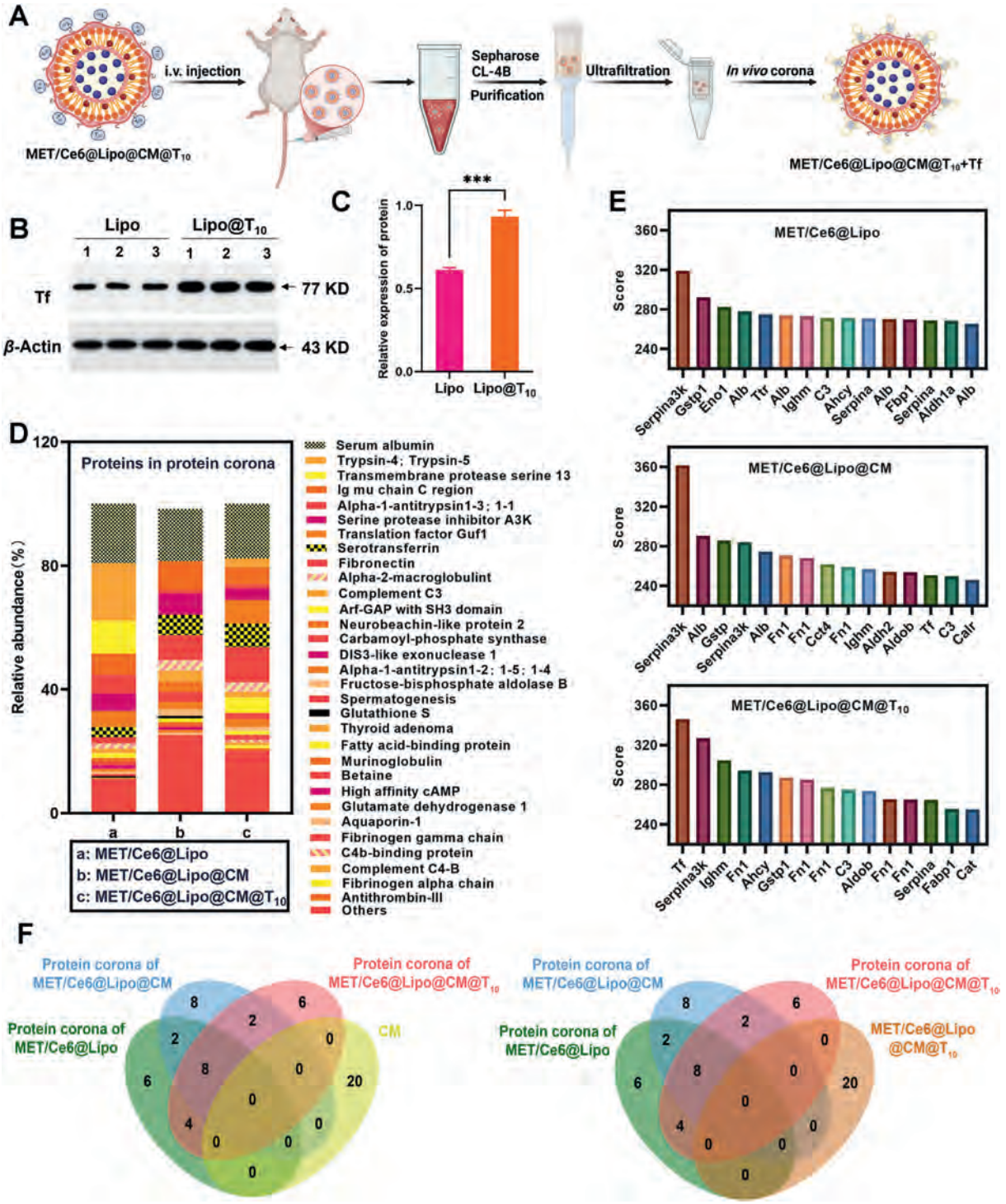

Figure 3 *In vivo* Tf binding and protein corona characterization of MET/Ce6@Lipo@CM@T_{10}. (A) Schematic description of the experimental design and preparation of *in vivo* protein corona formation. (B) WB measurement of Tf expression and (C) quantitative expression level on the surface of liposomes. Data are expressed as mean ± SD ($n = 3$), $^{*}P < 0.05$,$^{**}P < 0.01$,$^{***}P < 0.001$. (D) The most 20 abundant proteins identified in the protein corona of MET/Ce6@Lipo, MET/Ce6@Lipo@CM, and MET/Ce6@Lipo@CM@T_{10} by LC−MS/MS. (E) Scores of different genes identified in the protein corona of MET/Ce6@Lipo, MET/Ce6@Lipo@CM, and MET/Ce6@Lipo@CM@T_{10} by LC-MS/MS. (F) Overlap investigation of the top 20 proteins in different groups of formulations.

in vivo, confirming the successful formation of the Tf-protein corona (Tf-PC).

To further analyze the protein composition and relative abundance of Tf in the Tf-PC formed *in vivo*, we performed LC−MS/MS analysis. The top 20 proteins detected in each group are presented in Fig. 3D and Supporting Information Tables S1−S3. Serum albumin was the most abundant protein class in the Tf-PCs formed by all three groups. In the MET/Ce6@Lipo group, Tf

(serotransferrin) accounted for 3.22% of all proteins, ranking eighth. In the MET/Ce6@Lipo@CM group, Tf content increased to 6.54%, ranking fifth. Notably, in the MET/Ce6@Lipo@CM@T_{10} group, Tf accounted for 7.58% of all proteins, ranking third. Among the three groups, the T_{10}-modified lipo-complex exhibited the highest Tf content within the Tf-PC, consistent with the WB results.

We also compared the top 15 protein and gene scores obtained from the analysis (Fig. 3E). In the MET/Ce6@Lipo@CM@T_{10} group, Tf achieved the highest gene score, indicating that T_{10} effectively bound to Tf protein in plasma, forming a reliable and stable Tf-PC during circulation. By contrast, no Tf-related genes were observed in the top 15 scores for the MET/Ce6@Lipo group, while the Tf gene ranked 13th in the MET/Ce6@Lipo@CM group. The proteomics score, which reflects the reliability of protein identification, is derived from parameters such as spectral specificity and peptide numbers. A higher score suggests greater biological relevance and significance. These findings validated the ability of the T_{10} peptide to bind Tf *in vivo*, providing a solid theoretical and experimental foundation for further *in vivo* pharmacodynamics evaluations.

Furthermore, we determined the surface protein components of the extracted U87 cell membrane and final formulation of MET/Ce6@Lipo @ CM@T_{10}. The results are shown in the table and Figure below. Supporting Information Table S4 lists the names and types of the top 20 proteins that occupy the surfaces of MET/Ce6@Lipo@CM@T_{10} preparations. Tenascin, a cell surface fibronectin, is the protein with the highest occupancy among the two preparations, indicating that the proteins on the surfaces of the two preparations mainly come from the extracted cell membranes. As illustrated in Fig. 3F, there is no overlap of identifiable proteins among the top 20 protein types associated with CM or MET/Ce6@Lipo@CM@T_{10} and the top 20 surface proteins of the *in vivo*-formed protein corona. This lack of overlapping proteins suggests that neither the CM nor MET/Ce6@Lipo@CM@T_{10} formulation interferes with or influences the formation of these surface proteins *in vivo*.

3.4. Homologous targeting and cellular uptake analyses

Various membrane proteins and surface adhesion molecules from tumor cell membranes were preserved on the surface of the NPs, forming the basis of their homologous targeting ability. Protein components on the surface of the NPs were identified by SDS-PAGE. As shown in Supporting Information Fig. S3, no membrane protein components were present on the surface of MET/Ce6@Lipo. However, U87 cancer CM lysate, cancer CM vesicles, MET/Ce6@Lipo@CM, and MET/Ce6@Lipo@CM@T_{10} exhibited highly similar electrophoretic band patterns, confirming that the membrane proteins and adhesion molecules were successfully retained on the NPs and remained intact.

The cellular uptake of the lipo-complexes was first observed using CLSM (Fig. 4A). U87 CM was labeled with DiO (green fluorescence), and no green fluorescence signal was detected in the Ce6@Lipo group. By contrast, clear green fluorescence signals were observed in the Ce6@Lipo/DiO@CM and Ce6@Lipo/DiO@CM@T_{10} groups, indicating successful U87 CM coating. Among these groups, all formulations containing Ce6 exhibited red fluorescence signals, with Ce6@Lipo/DiO@CM showing the strongest signal (represented by strong yellow fluorescence). These results confirmed that the core−shell structure of the biomimetic nanomedicine successfully encapsulated therapeutic drugs, while the cell membrane coating extended blood circulation time and enhanced tumor-targeting ability. In addition, the strong yellow fluorescence signal in Ce6@Lipo/DiO@CM@T_{10} suggested that T_{10} modification did not hinder U87 cell uptake and that the lipo-complexes effectively delivered drugs following CM coating and T_{10} modification.

To further quantify cellular uptake, flow cytometry was used to determine the uptake percentages of different lipo-complex formulations (Fig. 4B). Compared with Ce6@Lipo, the uptake rates of Ce6@Lipo@CM and Ce6@Lipo@CM@T_{10} were significantly higher ($^{**}P < 0.01$). This improvement was attributed to the tumor CM coating, which enhanced internalization and homologous targeting. Furthermore, the Tf-incubated lipo-complex (Ce6@Lipo@CM@T_{10}+Tf) exhibited the highest uptake rate ($^{**}P < 0.01$ and $^{***}P < 0.001$). This result indicated that Ce6@Lipo@CM@T_{10} could bind to the TfR on the surface of U87 tumor cells, promoting active targeting and internalization. The combined effects of CM and T_{10} thus enhanced drug delivery efficiency to brain glioma cells in the complex blood environment.

3.5. ROS activity of Ce6 and the capacity of MET to relieve hypoxia

The production of high levels of ROS in tumor cells by photosensitizers is a key criterion for evaluating photodynamic efficiency. To assess the photodynamic effect of MET/Ce6@Lipo@CM@T_{10} under light irradiation, DCFH-DA was used as a ROS indicator. As shown in Fig. 5A and C, no significant difference in green fluorescence was observed between the PBS group and the PBS (L+) group, with only minimal green fluorescence detected in the MET@Lipo (L+) group, indicating that light alone had no significant impact on ROS production in cells without photosensitizers. However, all Ce6-containing groups displayed prominent green fluorescence in cells, confirming the photosensitizer activity of Ce6, which generated ROS under 640 nm light. Among these, the MET/Ce6@Lipo@CM (L+) and MET/Ce6@Lipo@CM@T_{10}+Tf (L+) groups exhibited the strongest green fluorescence intensity. This result demonstrates that homologous targeting by CM and active targeting by Tf enhance the uptake of lipo-complexes by tumor cells, leading to significant ROS production under light exposure.

Hypoxia is a hallmark of tumors, arising from their rapid proliferation and high metabolic rates[38,39]. During PDT, the oxygen-consuming process exacerbates intracellular hypoxia, which promotes tumor growth. MET, as an oxidative phosphorylation inhibitor, reduces mitochondrial respiration and mitigates hypoxia, enhancing the therapeutic effect of PDT. HIF-1α, a key transcription factor in hypoxic conditions, serves as a marker of hypoxia. Hypoxiaprobe-1, a hypoxia-sensitive indicator, binds HIF-1α and inhibits its activity to measure intracellular hypoxia. As shown in Fig. 5B and D, cells in the Ce6@Lipo (L+) group exhibited pronounced red fluorescence, indicating hypoxia. In comparison, the MET/Ce6@Lipo@CM (L+) group demonstrated significantly reduced red fluorescence, suggesting alleviated intracellular hypoxia. The MET/Ce6@Lipo@CM@T_{10}+Tf (L+) group exhibited the lowest red fluorescence intensity, indicating enhanced MET uptake *via* dual targeting, which effectively counteracted PDT-induced hypoxia and improved therapeutic outcomes.

The hypoxia-reversing effect of MET was further validated *via* WB (Fig. 5E and F). The Ce6@Lipo group showed the highest HIF-1α expression, reflecting severe hypoxia due to oxygen consumption following NIR irradiation. The addition of MET

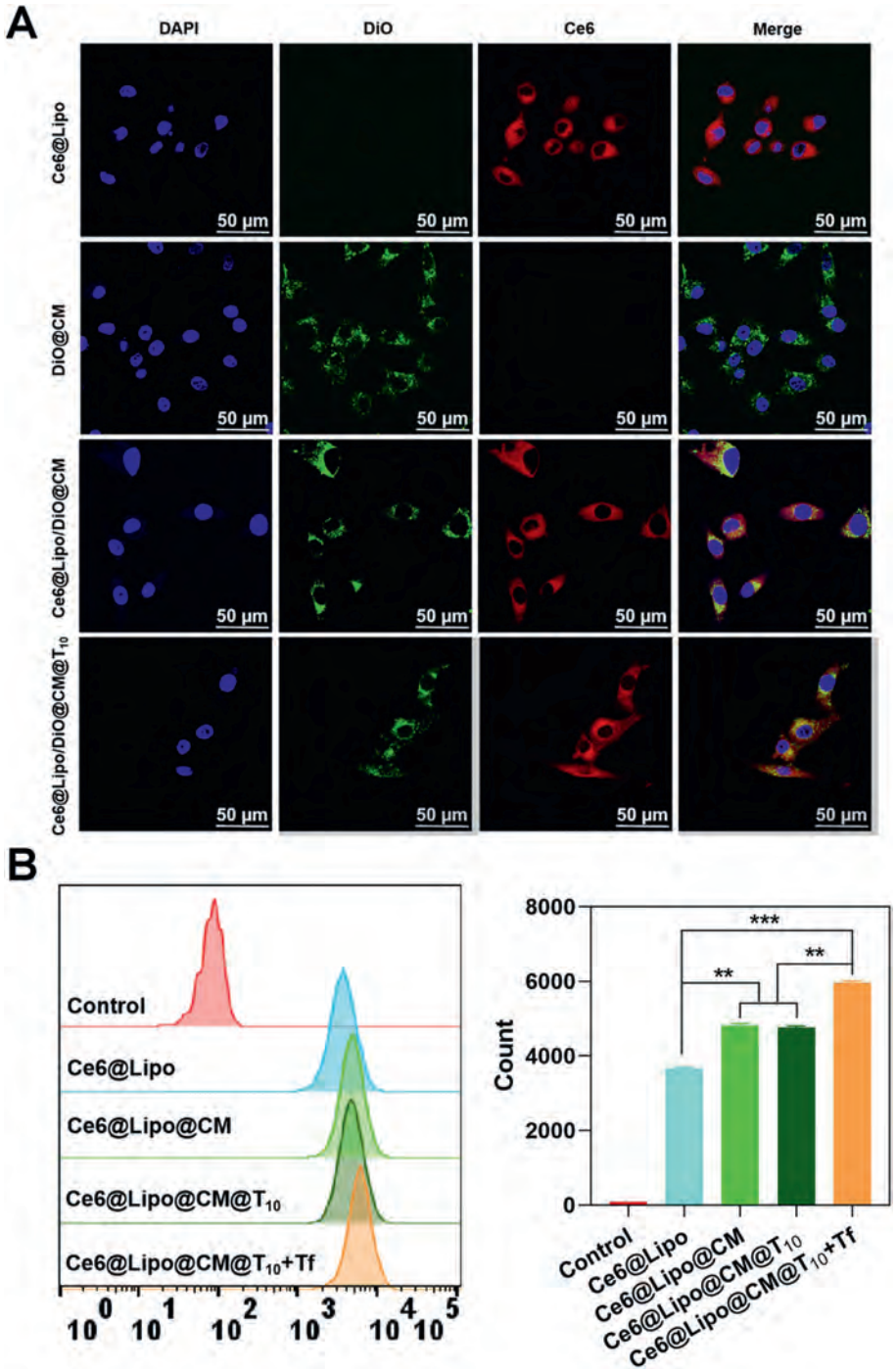

Figure 4 Cellular uptake assay. (A) Qualitative observation of Ce6@Lipo, DiO@CM, Ce6@Lipo/DiO@CM, and Ce6@Lipo/DiO@CM@T_{10} by CLSM. Scale bar: 50 μm. (B) Quantitative analysis of cellular uptake of Ce6@Lipo, Ce6@Lipo@CM, Ce6@Lipo@CM@T_{10}, and Ce6@Lipo@CM@T_{10}+Tf by flow cytometry.

reduced HIF-1α expression, consistent with prior experimental results, confirming its role in alleviating tumor hypoxia. Among all groups, MET/Ce6@Lipo@CM@T_{10}+Tf exhibited the lowest HIF-1α expression, indicating that MET in this preparation effectively reversed hypoxia, thereby improving PDT efficacy.

The MitoCheck Complex I Activity Detection Kit was used to investigate the effect of MET on mitochondrial complex I in U87 cells, reflecting mitochondrial respiratory chain activity. When tested under dark conditions, the activity of complex I in the MET/Ce6@Lipo@CM@T_{10}+Tf group (17.632 U/mg prot) was similar to that in the MET @Lipo group (19.202 U/mg prot) and significantly different from that in the MET/Ce6@Lipo@CM@T_{10} group (34.859 U/mg prot) (Fig. 5G). It is well known that Met has been proven to have the ability to reduce OCR by destroying mitochondrial complex I, thereby reversing tumor hypoxia[40,41]. To validate this, we investigated how co-

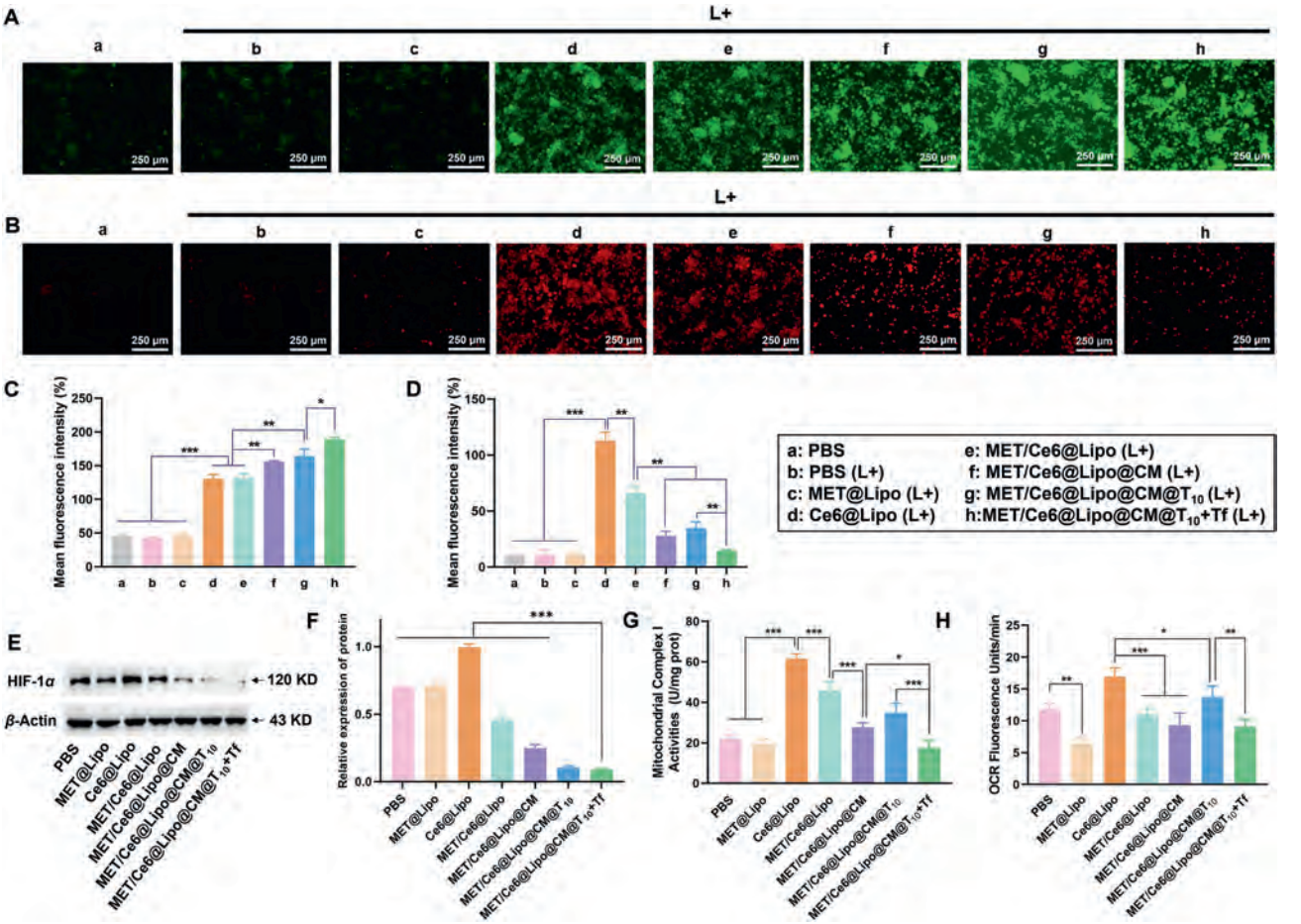

Figure 5 ROS activity of and hypoxic relieving capacity of MET/Ce6@Lipo@CM@T_{10}. (A) *In vitro* ROS generation induced by various treatments with or without irradiation. (B) *In vitro* hypoxia generation induced by various treatments with or without irradiation. (C) Quantitative analysis of *in vitro* ROS generation induced by various treatments with or without irradiation. (D) Quantitative analysis of *in vitro* hypoxia generation induced by various treatments with or without irradiation. (E) Determination of HIF-1α expression in U87 cells treated with different formulations by WB. (F) Quantitative expression level of HIF-1α in U87 cells treated with different formulations by WB. (G) Detection of mitochondrial respiratory complex I activity in U87 cells after treatment with different formulations. (H) Oxygen consumption rate (OCR) of U87 cells after treatment with different formulations. Data are expressed as mean ± SD ($n = 3$), $^{*}P < 0.05$, $^{**}P < 0.01$, and $^{***}P < 0.001$.

administration of MET and Ce6 formulations affects oxygen consumption and alleviates hypoxia. During laser irradiation, Ce6 preferentially consumes oxygen in the surrounding tissue, inducing hypoxia. Conversely, MET inhibits the respiratory chain, thereby alleviating hypoxia within the tumor microenvironment. As shown in Fig. 5H, MET/Ce6@Lipo@CM@T_{10}+Tf treated group significantly reduces U87 cell OCR compared with MET/Ce6@Lipo@CM@T_{10} (about 1.5-fold), indicating that Tf effectively binds to TfR on the surface of U87, improving drug uptake by cells and even alleviating hypoxia. Under the effective uptake mediated by receptors, the OCR in the MET/Ce6@Lipo@CM@T_{10}+Tf group was similar to that in the MET@Lipo group. These findings suggest that MET/Ce6@Lipo@CM@T_{10} exhibits significant hypoxia relief *in vivo*, which may contribute to enhancing its anti-tumor efficacy.

3.6. *PDT-induced immune activation*

Mitochondria, the primary organelles for cellular energy metabolism, are critical targets for PDT. High ROS levels can damage mitochondrial function, decrease membrane potential, activate apoptotic pathways, and ultimately induce tumor cell death[42,43]. Fig. 6A shows that red fluorescence, representing functional mitochondria, was prominent in the PBS and PBS (L+) groups, with minimal green fluorescence, indicating no mitochondrial damage due to light irradiation without a photosensitizer. MET, capable of inhibiting mitochondrial respiration[44,45], caused a moderate reduction in red fluorescence within the MET@Lipo treatment group, indicating moderate mitochondrial injury. By contrast, the MET/Ce6@Lipo@CM (L+) group exhibited significantly increased green fluorescence, indicating substantial mitochondrial damage, likely due to CM-mediated homologous targeting that enhanced drug delivery to cells. The MET/Ce6@Lipo@CM@T_{10}+Tf group showed the strongest green fluorescence signal, reflecting the synergistic effect of Tf targeting and homologous targeting, which amplified PDT efficacy and caused severe mitochondrial damage, leading to tumor cell apoptosis.

HMGB1, a nuclear protein involved in DNA regulation and repair, is released into the extracellular environment during cell death. The release of HMGB1 due to PDT-induced cell damage triggers immune recognition and promotes an immune response.

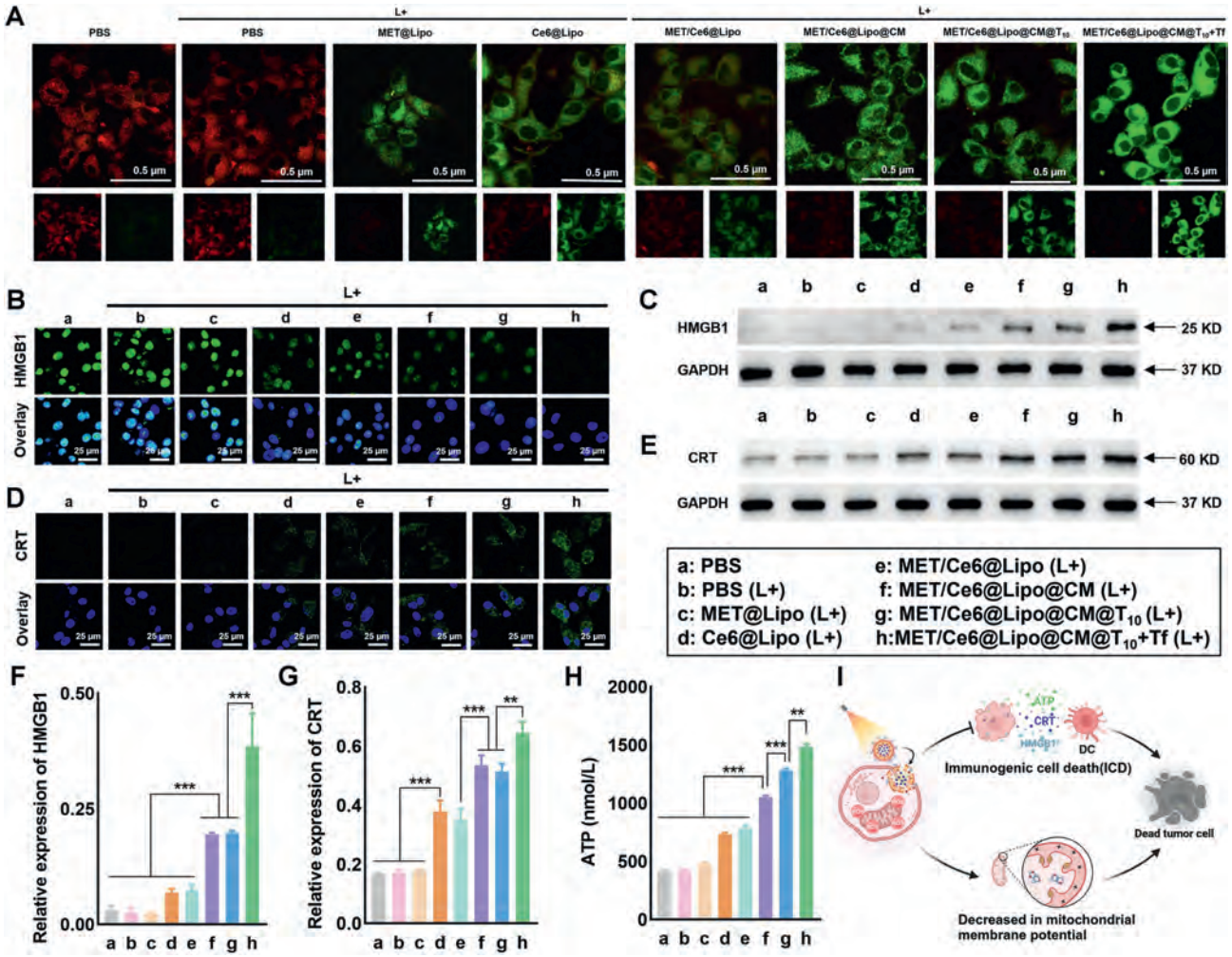

Figure 6 Photodynamic performance and immune activation *in vitro*. (A) JC-1 fluorescence for characterization of mitochondrial membrane potential after U87 cells under various formulations determined by CLSM. (B) Immunofluorescence staining of HMGB1 in U87 cells after various formulations with or without irradiation. The cell nuclei were stained by DAPI. Scale bar: 25 μm. (C) Determination of HMGB1 expression in U87 cells treated with different formulations by WB. (D) Immunofluorescence staining of CRT in U87 cells after various formulations with or without irradiation. The cell nuclei were stained by DAPI. Scale bar: 25 μm. (E) Determination of CRT expression in U87 cells treated with different formulations by WB. (F) Quantitative expression level of HMGB1 in U87 cells treated with different formulations by WB. (G) Quantitative expression level of CRT in U87 cells treated with different formulations by WB. (H) ATP release from U87 cells under various formulations with or without irradiation. Data are expressed as mean ± SD ($n = 3$), $^{***}P < 0.001$. (I) Schematic illustration of ICD effect induced by MET/Ce6@Lipo@CM@T_{10} under irradiation.

CLSM was used to detect extracellular HMGB1 released from tumor cells (Fig. 6B). In the PBS, PBS (L+), and MET@Lipo (L+) groups, green fluorescence signals overlapped with blue DAPI fluorescence in the nucleus, indicating that HMGB1 remained intracellular. By contrast, all Ce6-containing groups showed reduced green fluorescence in the nucleus after light exposure, indicating HMGB1 release into the extracellular environment. The MET/Ce6@Lipo@CM@T_{10}+Tf (L+) group exhibited the weakest nuclear green fluorescence, suggesting the highest extracellular HMGB1 release among all groups.

CRT, an endoplasmic reticulum calcium-binding protein, translocates to the CM surface under oxidative stress or cell damage, marking cells for immune detection following PDT-induced death. As shown in Fig. 6D, the PBS, PBS (L+), and MET@Lipo (L+) groups exhibited minimal green fluorescence, while MET/Ce6@Lipo@CM (L+), MET/Ce6@Lipo@CM@T_{10} (L+), and MET/Ce6@Lipo@CM@T_{10}+Tf (L+) groups displayed strong green fluorescence signals. This indicates that light-induced PDT promoted CRT exposure on tumor cell surfaces in these groups.

Furthermore, we conducted WB experiments to investigate the HMGB1 and CRT of U87 cells after treatment with different preparations on. As shown in Fig. 6C and F, we investigated the ability of U87 cells to release HMGB1 after stimulation with different preparations. After recovering the culture medium treated with different groups, the expression of HMGB1 in the culture solution was determined. The results showed that there was no significant difference in the expression of HMGB1 among PBS, MET@Lipo, Ce6@Lipo, or MET/Ce6@Lipo groups. This may be due to the limited release of HMGB1 in the culture medium, and there may not be a significant difference. However, formulations coated with CM or modified with T_{10} can

significantly stimulate and release HMGB1 from cells. Moreover, the Tf incubated group showed significant differences compared to the CM and T_{10} modified groups, with the highest release of HMGB1. Fig. 6E and G shows the WB experimental results of CRT factor. From the result graph, we can see that there are significant differences in CRT content among different groups of cells stimulated by different preparations. Compared with the PBS or MET@Lipo groups, the expression of CRT in the Ce6@Lipo and Lipo@Lipo groups was significantly increased, and similar to the HMGB1 experimental results. The Tf incubation group had the highest expression of CRT on the cell surface among all groups, which is consistent with the immunofluorescence analysis results in Fig. 6D.

ATP, the primary cellular energy molecule, is released extracellularly during PDT-induced cell death. ATP release serves as a damage signal to the immune system, promoting antigen presentation and T-cell activation. As shown in Fig. 6H, ATP levels were highest in the MET/Ce6@Lipo@CM@T_{10}(L+) group, demonstrating significant differences compared with other groups. This indicates that MET/Ce6@Lipo@CM@T_{10} induced a strong PDT effect, leading to substantial ATP release and immune activation.

The schematic in Fig. 6I illustrates the process by which tumor cells transition from non-immunogenic to immunogenic states, initiating an anti-tumor immune response. This transition, known as immunogenic cell death (ICD), is triggered by external stimuli such as PDT and results in the release of damage-associated molecular patterns (DAMPs). DAMPs, including CRT, HMGB1, and ATP, are critical mediators of anti-tumor immunotherapy[46]. CRT stimulates DC phagocytosis, ATP recruits DCs to the tumor site, and HMGB1 enhances stable interactions between DCs and dying tumor cells, facilitating T-cell activation and anti-tumor immunity. We incubated tumor cells with various drug formulations to assess their ability to induce ICD by measuring CRT translocation, as well as HMGB1 and ATP secretion levels. Experimental data demonstrated that MET/Ce6@Lipo@CM@T_{10} enhanced ICD by disrupting tumor cell metabolism and inducing a robust PDT effect.

3.7. In vitro anti-tumor efficacy analyses

We first evaluated the cytotoxicity of Blank Lipo, Blank Lipo@CM, and Blank Lipo@CM@T_{10} using the CCK-8 assay. The survival rate of U87 cells in all three groups exceeded 90% (Supporting Information Fig. S4), indicating that the blank vectors exhibited minimal toxicity and could serve as safe delivery systems for GBM treatment. To assess the *in vitro* inhibitory effect of different formulations on U87 cells, we evaluated cell inhibition rates under conditions with and without laser irradiation. As shown in Fig. 7A, in the absence of irradiation, the survival rate of U87 cells remained above 85% after 24 h of incubation with each drug formulation, indicating that these lipo-complexes exhibited low cytotoxicity without light activation. Upon laser irradiation, all groups containing Ce6 photosensitizers demonstrated significant cytotoxicity, confirming the potent anti-tumor effects induced by PDT. Notably, the MET/Ce6@Lipo@CM group exhibited a higher cell inhibition rate than the Ce6@Lipo and MET/Ce6@Lipo groups, which can likely be attributed to enhance homologous targeting conferred by the tumor CM coating. Furthermore, the T_{10}-modified MET/Ce6@Lipo@CM@T_{10} group demonstrated the lowest U87 cell survival rate after laser irradiation.

Given these results, we hypothesized that during incubation, T_{10} might bind to Tf in the culture medium, thereby facilitating cellular uptake of the lipo-complexes and enhancing their inhibitory effect on cell proliferation. To validate the role of Tf in targeting tumor cells, we compared the inhibitory effects of MET/Ce6@Lipo@CM@T_{10} and MET/Ce6@Lipo@CM@T_{10}+Tf at various concentrations. As shown in Fig. 7B, the inhibitory effects of both formulations on U87 cell proliferation increased with Ce6 concentration, exhibiting dose-dependence. At equivalent drug concentrations, the MET/Ce6@Lipo@CM@T_{10}+Tf group showed significantly greater inhibition than MET/Ce6@Lipo@CM@T_{10}, confirming that Tf binding played a critical role in active targeting and further improved the cell inhibition rate.

The apoptosis of U87 cells induced by different lipo-complexes was evaluated using flow cytometry. As shown in Fig. 7C and D, the apoptosis rates for the PBS, PBS (L+), and MET@Lipo (L+) groups were 13.36 ± 1.08%, 13.08 ± 2.10%, and 17.19 ± 0.80%, respectively. By contrast, the apoptosis rates for Ce6@Lipo (L+), MET/Ce6@Lipo (L+), MET/Ce6@Lipo@CM (L+), and MET/Ce6@Lipo@CM@T_{10} (L+) groups were 28.8 ± 2.03%, 30.2 ± 2.5%, 40.8 ± 1.8%, and 47.0 ± 0.8%, respectively. These findings align with the results of the cell proliferation inhibition assays, indicating that Ce6-containing NPs activated PDT under light exposure and induced tumor cell apoptosis. Notably, the MET/Ce6@Lipo@CM@T_{10}+Tf (L+) group exhibited the highest apoptosis rate 65 ± 1.02%, suggesting that its active targeting mechanism, facilitated by Tf binding, enhanced cellular uptake and apoptosis induction.

The anti-tumor effects of the different formulations were further assessed using live-cell staining. As shown in Fig. 7E and F, the green fluorescence signal indicating viable cells was weakest in the MET/Ce6@Lipo@CM@T_{10}(L+) group, demonstrating its superior tumor cell-killing ability. This result was consistent with the CCK-8 assay and apoptosis analysis, further confirming the potent anti-tumor efficacy of MET/Ce6@Lipo@CM@T_{10} in inhibiting tumor cell growth. Using a normal cell line with low TfR expression for CCK-8 cytotoxicity evaluation can highlight the targeting specificity of the preparations. Based on our research of two papers[47,48], we selected Caco-2 cells and bEnd.3 cells with low TfR expression as models to evaluate the cell inhibition efficacy of MET/Ce6@Lipo@CM@T_{10} and MET/Ce6@Lipo@CM@T_{10}+ Tf. As shown in Supporting Information Fig. S5, there was no significant difference in cell inhibition rate between Caco-2 cells and bEnd.3 cells at the same concentration, while the cell inhibition rate in the Tf-added group was slightly weaker. This is because the TfR on the surface of these two cell lines is relatively low, which does not facilitate effective uptake mediated by Tf. Instead, the increased Tf acts as a high molecular weight protein, hindering the entry of the formulation into the cell, resulting in a lower cell inhibition rate of the formulation after Tf incubation.

3.8. Evaluation of blood−brain barrier and tumor tissue penetration activity in vitro

Penetrating the BBB and delivering therapeutic agents to brain tumors remain significant challenges in glioblastoma treatment. It is known that Tf can enter the brain *via* receptor-mediated endocytosis by binding specifically to TfR on the BBB surface. We hypothesized that Ce6@Lipo@CM@T_{10} could cross the BBB through TfR-mediated endocytosis. To test this, we established an

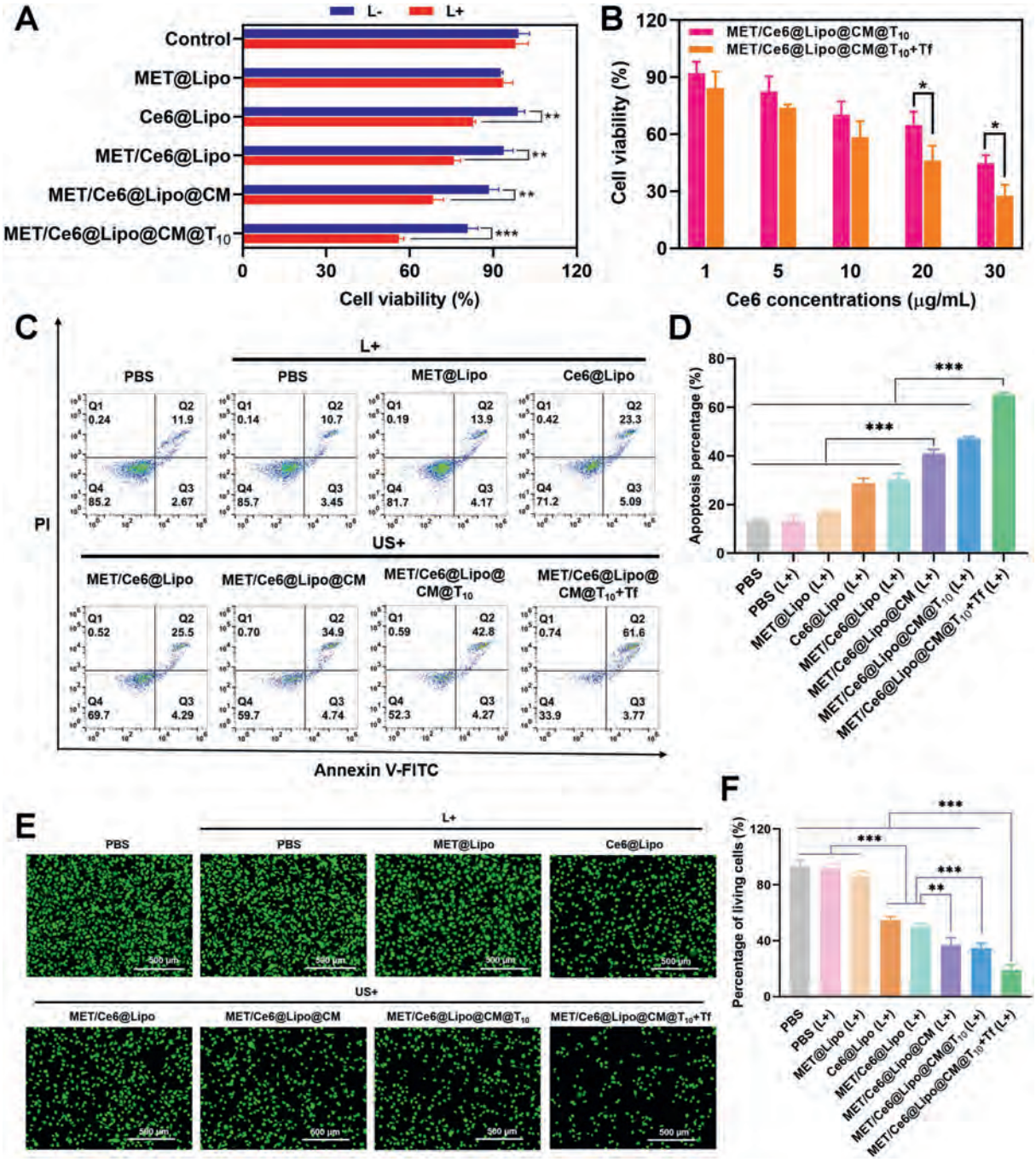

Figure 7 *In vitro* anti-cancer efficacy of MET/Ce6@Lipo@CM@T_{10}. (A) Cell viability of 4T1 cells after incubation with different formulations with or without laser irradiation (640 nm, 100 W/cm^2, 5 min). (B) Different concentrations of MET/Ce6@Lipo@CM@T_{10} and MET/Ce6@Lipo@CM@T_{10}+Tf incubation inhibits the proliferation of U87 under irradiation. (C, D) Cell apoptosis induced by various formulations with laser irradiation examined by flow cytometry. The cells were stained with Annexin V-FITC and PI. (E, F) Live examination of U87 cells subjected to different formulations was conducted by Calcein-AM staining and observed by fluorescence microscope (Scale bar: 500 μm). Data are expressed as mean ± SD ($n = 3$), *$P < 0.05$, **$P < 0.01$, ***$P < 0.001$.

in vitro BBB model to evaluate the ability of Ce6@Lipo@CM@T_{10} to traverse the BBB and target brain tumor cells. As illustrated in the schematic diagram (Fig. 8A), bEnd.3 cells were seeded in the upper chamber and U87 cells in the lower chamber of a Transwell system, mimicking the *in vivo* BBB and brain tumor environment, respectively. TEER values were measured to confirm successful model establishment. When the TEER value reached 200, different formulations were added to the upper chamber to investigate their ability to penetrate the bEnd.3 barrier and target U87 cells in the lower chamber[49]. Fig. 8B shows three-dimensional fluorescence imaging of the bEnd.3 cell layer in the Transwell model. Free Ce6 exhibited weak red fluorescence in the lower U87 cell layer, indicating limited penetration ability. By contrast, the Ce6@Lipo@CM group displayed stronger red

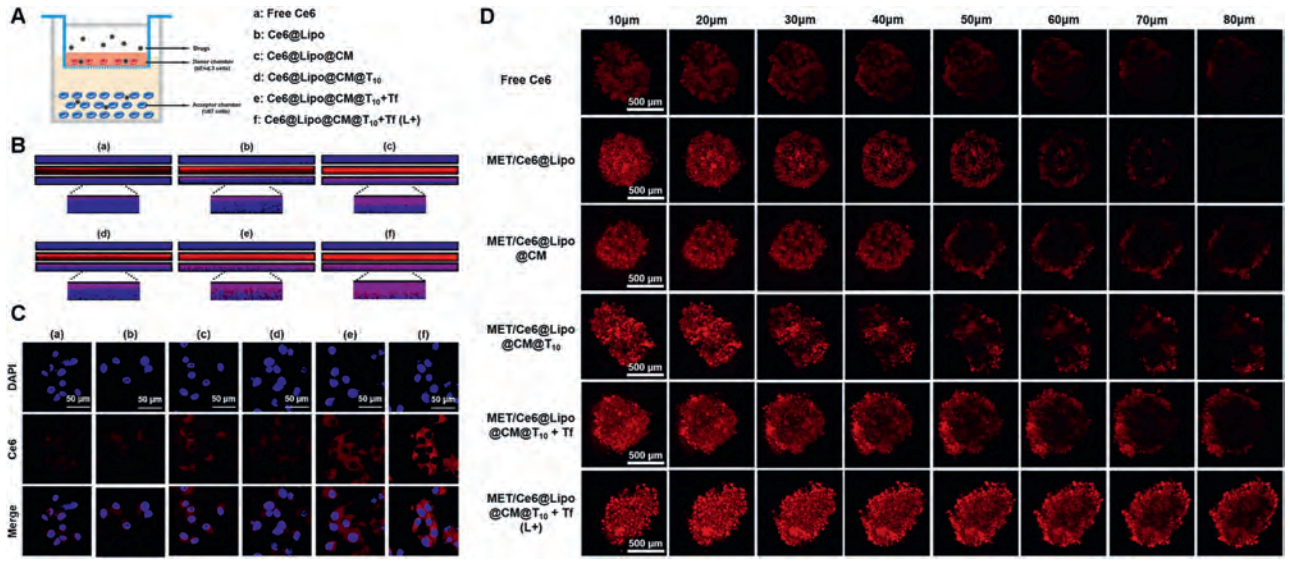

Figure 8 *In vitro* blood−brain barrier (BBB) transcytosis. (A) The BBB model was established *in vitro*. (B) Three-dimensional fluorescence imaging of CLSM in the bEnd.3 cell layer in the upper chamber of transwell was shown as DAPI, Ce6, Merge, with cell layer thickness of 50 μm. (C) Fluorescence images in acceptor chamber (blue: DAPI; red: Ce6). Scale bar: 50 μm. (D) Fluorescence imaging of U87 spheroids at increasing depth treated with different lipo-complexes (red: Ce6). Scale bar: 250 μm.

fluorescence, suggesting enhanced BBB penetration due to the homologous targeting effect of the tumor cell membrane coating. However, the fluorescence intensity of the Ce6@Lipo@CM@T_{10} group was reduced compared with Ce6@Lipo@CM, indicating that T_{10} modification without exogenous Tf addition impaired BBB crossing ability. Notably, the fluorescence intensity in the Ce6@Lipo@CM@T_{10}+Tf and Ce6@Lipo@CM@T_{10}+Tf (L+) groups was significantly enhanced compared with other groups. In particular, the Ce6@Lipo@CM@T_{10}+Tf (L+) group exhibited the strongest fluorescence signal, covering the entire bEnd.3 cell layer. These results demonstrate that the addition of exogenous Tf improved BBB penetration, especially after laser irradiation, further enhancing the active targeting capability of the lipo-complexes. Fig. 8C shows CLSM images of U87 cells in the lower chamber. Free Ce6 and Ce6@Lipo groups exhibited weak red fluorescence, indicating poor uptake by U87 cells through the BBB. By contrast, the Ce6@Lipo@CM group showed stronger red fluorescence, suggesting that the tumor CM coating facilitated BBB penetration to some extent. However, the Ce6@Lipo@CM@T_{10} group exhibited reduced fluorescence intensity compared with Ce6@Lipo@CM, likely due to the T_{10} modification obstructing the surface coating in the absence of serum, thereby diminishing the homologous targeting capability of the lipo-complexes. The fluorescence intensity of Ce6@Lipo@CM@T_{10}+Tf and Ce6@Lipo@CM@T_{10}+Tf (L+) groups was significantly higher than other groups, with Ce6@Lipo@CM@T_{10}+Tf (L+) showing the strongest signal. These findings indicate that exogenous Tf facilitated the formation of a transferrin crown on the lipo-complex surface, significantly enhancing BBB penetration, particularly after laser irradiation. This improved efficiency in crossing the BBB enabled more effective targeting of brain glioma.

To better simulate the tumor microenvironment, a 3D tumor spheroid model of U87 cells was established to study the permeability of MET/Ce6@Lipo@CM@T_{10}. The permeability of U87 cell spheroids was assessed by treating them with different NPs and applying laser irradiation. The fluorescence intensity of the spheroids at depths of 10−80 μm was observed using CLSM. As shown in Fig. 8D, due to the low solubility of free Ce6 and the lack of specific targeting function, the overall fluorescence signal of the Free Ce6 group is relatively weak. The fluorescence signals and permeation efficiency of MET/Ce6@Lipo, MET/Ce6@Lipo@CM, and MET/Ce6@Lipo@CM@T_{10} groups are generally similar, and compared with the MET/Ce6@Lipo@CM@T_{10}+Tf group, the tumor sphere permeation ability is weaker. Under laser irradiation, the fluorescence intensity in the MET/Ce6@Lipo@CM@T_{10}+Tf (L+) group increased significantly compared with the MET/Ce6@Lipo@CM@T_{10}+Tf group without irradiation. The fluorescence in the middle position of the tumor sphere began to disappear in the unirradiated Tf group at 50 μm, but decreased in the irradiated Tf group at 70 μm. Laser irradiation further promoted the penetration of lipo-complexes into tumor spheroids and enhanced drug accumulation within the tumor spheroids. These findings suggest that this nanomaterial-based drug delivery system has significant potential for the targeted therapy of brain tumors.

3.9. In vivo targeting study

An orthotopic U87-Luc GBM mouse model was established *via* brain stereotaxic injection, and the success of the model was confirmed using small animal live imaging and pathological sections. As shown in Supporting Information Fig. S6, extensive tumor cells were observed in the brain tissue of the mice, with tumor regions successfully established, demonstrating the feasibility of the model for subsequent *in vivo* distribution and pharmacodynamics studies.

To investigate the *in vivo* distribution of the lipo-complexes, different formulations were administered *via* tail vein injection, and their distribution was observed using small animal imaging at predetermined time points (2, 4, 6, 8, and 24 h). The focus was on the ability of the lipo-complexes to penetrate the BBB, target gliomas, and distribute to other major organs. As shown in Fig. 9A and B, the fluorescence intensity at brain tumor sites was higher in

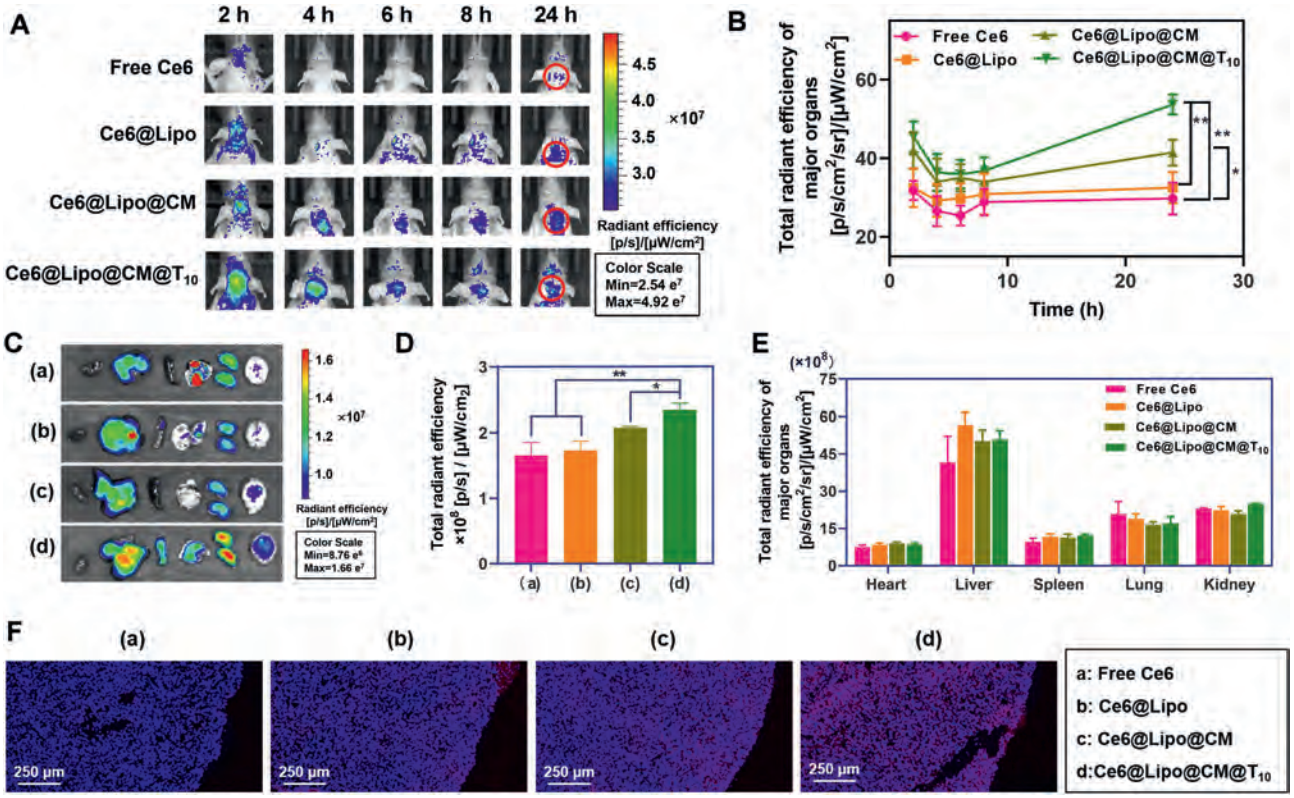

Figure 9 *In vivo* brain targeting and tumorous penetration efficacy. Brain tumor imaging (A) and fluorescence intensity (B) of mice at different time points after intravenous injection of free Free Ce6, Ce6@Lipo, Ce6@Lipo@CM, and Ce6@Lipo@CM@T_{10}. Fluorescence intensity (C) and quantitative analysis of the kinetic fluorescence intensity (D, E) of Ce6 in isolated tumors and major organs. (F) The distribution and penetration in tumor tissues determined by CLSM imaging of frozen tumor sections (Scale bar: 250 μm). Tumor cell were stained blue with DAPI. Data are expressed as mean ± SD, ($n = 3$), $P < 0.05$, $^{**}P < 0.01$.

the Ce6@Lipo@CM@T_{10} group compared with the free Ce6, Ce6@Lipo, and Ce6@Lipo@CM groups. The Ce6@Lipo@CM group exhibited increased fluorescence intensity at all-time points compared with the free Ce6 and Ce6@Lipo groups. While the fluorescence intensity in the free Ce6 and Ce6@Lipo groups decreased after 24 h, the fluorescence intensity in the Ce6@Lipo@CM group remained stable, suggesting that the U87 tumor CM coating enhanced nanoparticle accumulation and retention at the tumor site.

Previous studies have shown that tumor CM possess specific antigens and adhesion molecules (*e.g.*, proteins and polysaccharides) that facilitate homing, adhesion, and homologous targeting within tumor tissues, contributing to tumor growth and proliferation—a phenomenon known as "homologous adhesion properties"[34,50]. By mimicking these characteristics, tumor CM-coated biomimetic nanomaterials exhibit superior homologous targeting, enhancing drug enrichment at tumor sites and improving antitumor efficacy. In addition, compared with the Ce6@Lipo@CM group, the Ce6@Lipo@CM@T_{10} group demonstrated significantly higher fluorescence intensity at all-time points, which increased further over time. This suggests that the Tf-rich crown formed on Ce6@Lipo@CM@T_{10} extended the *in vivo* circulation time, enhanced brain targeting, and improved the accumulation and retention of the nanodrug at tumor sites, consistent with the results from the *in vitro* BBB endocytosis study.

Mice were sacrificed 24 h after tail vein injection, and the fluorescence intensity of various tissues, including the brain, heart, liver, spleen, lungs, and kidneys, was measured (Fig. 9C). Quantitative analysis of brain fluorescence intensity revealed that the Ce6@Lipo@CM@T_{10} group exhibited the highest fluorescence intensity among all groups, with a significant difference compared with the free Ce6, Ce6@Lipo, and Ce6@Lipo@CM groups (Fig. 9D). These results align with the *in vivo* imaging findings. And the liver, being the primary metabolic organ, exhibited the highest accumulation of the preparations, with minimal accumulation in other organs (Fig. 9E). These findings demonstrate that tumor CM-coated and T_{10}-modified nanoparticles enhance BBB penetration and drug retention at glioma sites following intravenous administration. Similar results were observed in previous cell uptake and BBB permeability studies. In addition, the tumor cell membrane coating prevents clearance by the phagocytic system in systemic circulation, thereby extending circulation time. This is evidenced by the sustained fluorescence intensity over 24 h, which contributes to improved drug efficacy. The formation of a transferrin crown on T_{10}-modified lipo-complexes through specific Tf adsorption mediates the efficient delivery of Ce6-containing lipo-complexes to the brain, enhancing tumor site aggregation and confirming the feasibility of active targeting *via* T_{10}-mediated endogenous Tf-PC.

To further evaluate *in vivo* targeting and tumor penetration, brain tissues were dissected and frozen sections prepared 3 h after tail vein administration of the various formulations. The distribution of the formulations within tumor tissues was observed using CLSM (Fig. 9F). Due to poor BBB penetration and low brain targeting, the free Ce6 and Ce6@Lipo groups exhibited

negligible red fluorescence signals in the glioma region. By contrast, the Ce6@Lipo@CM and Ce6@Lipo@CM@T_{10} groups displayed detectable red fluorescence signals in the glioma region. The Ce6@Lipo@CM@T_{10} group demonstrated a broader red fluorescence area and stronger intensity compared with the Ce6@Lipo@CM group, with significant fluorescence signal distribution even in deeper tumor regions. These results align with the findings from the *in vitro* 3D tumor spheroid study, providing a solid foundation for subsequent therapeutic evaluations in the mouse glioma model.

3.10. Evaluation of in vivo anti-tumor efficacy

On the 10th day after establishing the orthotopic GBM model, mice with uniform fluorescence intensities were randomly assigned to different treatment groups. Treatments included PBS, PBS(L+), MET@Lipo(L+), Ce6@Lipo(L+), MET/Ce6@Lipo (L+), MET/Ce6@Lipo@CM(L+), and MET/Ce6@Lipo@CM@T_{10}(L+), administered *via* tail vein injection (Ce6 dose: 2.5 mg/kg; MET dose: 10 mg/kg). Six hours after each injection, mice were irradiated with a 640 nm laser (0.8 W/cm^2) for 5 min. Drug administration occurred every three days for a total of five doses. Brain tumor growth was monitored on Days 10, 17, and 24 post-inoculation using small animal live imaging (Fig. 10A). As shown in Fig. 10B and C, within 15 days of treatment and laser irradiation, brain gliomas exhibited varying degrees of growth inhibition across the groups. On Day 24 post-inoculation, no significant difference in fluorescence intensity was observed between the PBS control group and the PBS (L+) group, indicating that light irradiation alone had no inhibitory effect on tumor cells. The MET@Lipo (L+) group exhibited strong fluorescence intensity, with tumors infiltrating most of the brain tissue. The Ce6@Lipo group showed PDT effects after irradiation, which inhibited tumor growth. The MET/Ce6@Lipo(L+) group demonstrated enhanced tumor inhibition compared with the Ce6@Lipo(L+) group, likely due to MET's ability to alleviate hypoxia in tumor tissues, hinder tumor cell growth, and enhance PDT efficacy. Compared with the PBS, PBS(L+), MET@Lipo (L+), Ce6@Lipo(L+), and MET/Ce6@Lipo(L+) groups, the MET/Ce6@Lipo@CM(L+) group exhibited weaker brain fluorescence intensity and significant antitumor effects, confirming that nanoparticles coated with tumor CMs possess excellent homologous targeting capabilities. Through effective enrichment at the tumor site *via* crossing the BBB, the drug is released, leading to its anti-tumor effect. Among all groups, the fluorescence signal in the MET/Ce6@Lipo@CM@T_{10} (L+) group was the weakest, indicating the most significant anti-tumor efficacy. The H&E staining results of brain tissues from different groups corroborated the fluorescence intensity findings. As shown in the H&E structural images in Fig. 10D, the tumors in the MET/Ce6@Lipo@CM@T_{10} (L+) group had the smallest area and the weakest invasion. The *in vivo* distribution experiments further demonstrated that the membrane-coated nanoparticles utilized their homologous camouflage properties to evade macrophage clearance after tail vein injection. This allowed them to cross the BBB and enter the brain. During circulation, the T_{10}-modified lipo-complex forms a transferrin corona with endogenous Tf, enabling dual-targeting functionality. It recognizes Tf receptors on the BBB surface to facilitate BBB crossing and binds to Tf receptors on brain tumor cells, entering the cells *via* endocytosis to release the drug payload. Thus, MET/Ce6@Lipo@CM@T_{10} enhances the PDT effect and achieves tumor inhibition through a combination of homologous CM-coated passive targeting and T_{10}-mediated active targeting. Additionally, we examined the potential hemorrhage risk of PDT on brain tissue during treatment. As shown in Supporting Information Fig. S7, PDT irradiation did not result in significant hemorrhage of the brain tissue.

TUNEL fluorescence analysis of embedded brain tissue (Fig. 10E and Supporting Information Fig. S8) revealed green fluorescence signals in all groups containing Ce6, indicating varying degrees of apoptosis and confirming the PDT efficacy of Ce6 under light exposure. The MET/Ce6@Lipo@CM (L+) group showed the largest area of TUNEL-positive cells compared with the Ce6@Lipo and MET/Ce6@Lipo (L+) groups, suggesting enhanced tumor cell apoptosis. Among all groups, MET/Ce6@Lipo@CM@T_{10} (L+) exhibited the strongest green fluorescence intensity ($^*P < 0.05$ when compared with MET/Ce6@Lipo@CM group), indicating the highest level of tumor cell apoptosis. H&E staining further confirmed these findings, with a significant reduction in tumor cells and visible necrosis and atrophy in the MET/Ce6@Lipo@CM@T_{10} (L+) group, demonstrating its ability to inhibit tumor proliferation and promote apoptosis.

Immunofluorescence staining for HIF-1α in tumor tissues was performed to assess whether hypoxia was alleviated. The results showed significantly reduced HIF-1α expression in the MET/Ce6@Lipo@CM@T_{10} (L+) group compared with other groups, consistent with *in vitro* cell-level experiments. Tumor cell proliferation and PDT-induced oxygen consumption often lead to severe hypoxia, which further promotes tumor growth. *In vitro* experiments demonstrated that MET/Ce6@Lipo@CM@T_{10} nanoparticles, through the inclusion of MET, inhibited oxygen consumption in tumor cells, alleviating hypoxia and enhancing PDT efficacy. These findings were validated *in vivo*, where MET was shown to mitigate PDT-induced hypoxia, thereby enhancing the antitumor efficacy of Ce6.

PDT is a non-invasive tumor treatment technique that generates ROS by locally stimulating photosensitizers, causing damage to cancer cells while reducing damage to normal tissues. This characteristic makes PDT a focus of attention for researchers and clinical doctors, especially in the treatment of brain tumors[51]. Photodynamic depth is a key challenge in the treatment of glioblastoma[52]. The lesion area is far away from the skin and peripheral blood vessels, coupled with the characteristics of brain tissue itself, which significantly reduces the transmission and accumulation of light energy[53,54]. In addition, photosensitizers in modern PDT systems often require local injection or exogenous application, which further increases the problem of insufficient depth. Therefore, developing new photosensitizers with stronger light absorption properties to improve the transmission and efficiency of light energy, or developing a new generation of multifunctional nanomaterials that can simultaneously emit light and have a killing effect on tumor cells, are some effective strategies to address this limitation. We used Ce6, which has both luminescence and anti-tumor efficacy, as a model drug, co loaded with hypoxia reliever MET, and utilized a highly targeted delivery system to address the limitations of PDT in the treatment of glioblastoma, achieving good anti-tumor results.

3.11. In vivo safety evaluation

The *in vivo* biosafety of the composite system was assessed using body weight monitoring, liver and kidney function tests, and H&E staining of major organs. Body weight changes were monitored

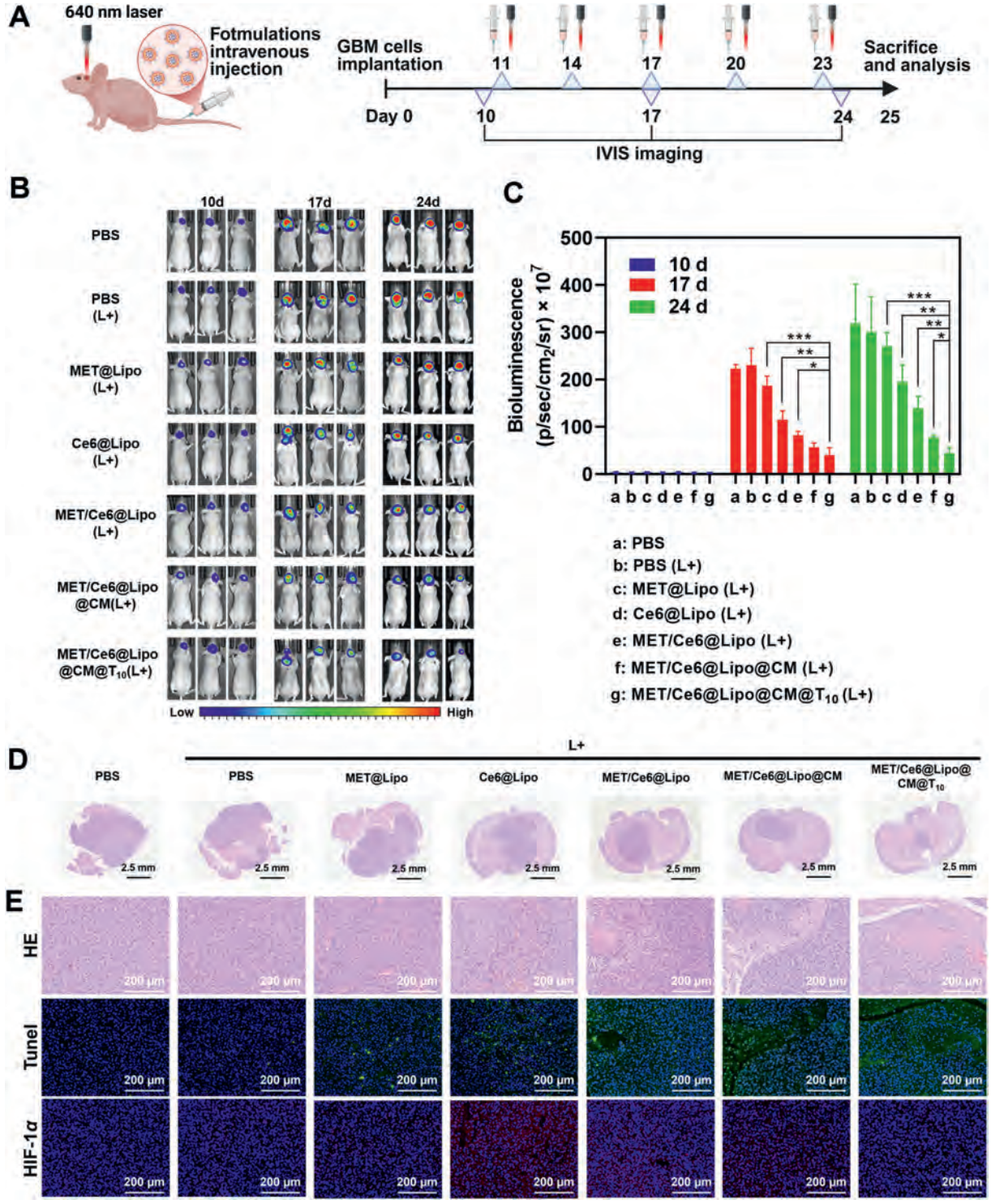

Figure 10 *In vivo* antitumor efficacy of MET/Ce6@Lipo@CM@T_{10}. (A) Schematic illustration of drug administration and irradiation in animals. (B) *In vivo* bioluminescence imaging of U87 brain tumor-bearing mice. (C) The relative quantification of the bioluminescence in tumors from the indicated treatment groups on the 10th, 17th, and 24th days. (D) H&E staining of brain sections treated with different formulations. (E) H&E staining, TUNEL detection and HIF-1α expression were detected in different groups of brain tumors with a scale of 200 μm. Data are expressed as mean ± SD, ($n = 3$), *$P < 0.05$, **$P < 0.01$, ***$P < 0.001$.

during tumor progression and treatment to evaluate systemic toxicity and tumor development. As shown in Fig. 11A, the weight of mice treated with MET/Ce6@Lipo@CM@T_{10} (L+) stabilized over time and was higher than that of other groups, indicating low systemic toxicity and a safe, effective targeted nano-delivery system. Liver function (ALT, AST) and kidney function (BUN, CRE) were assessed through serum biochemical analysis (Fig. 11B). The results showed that all values remained within the

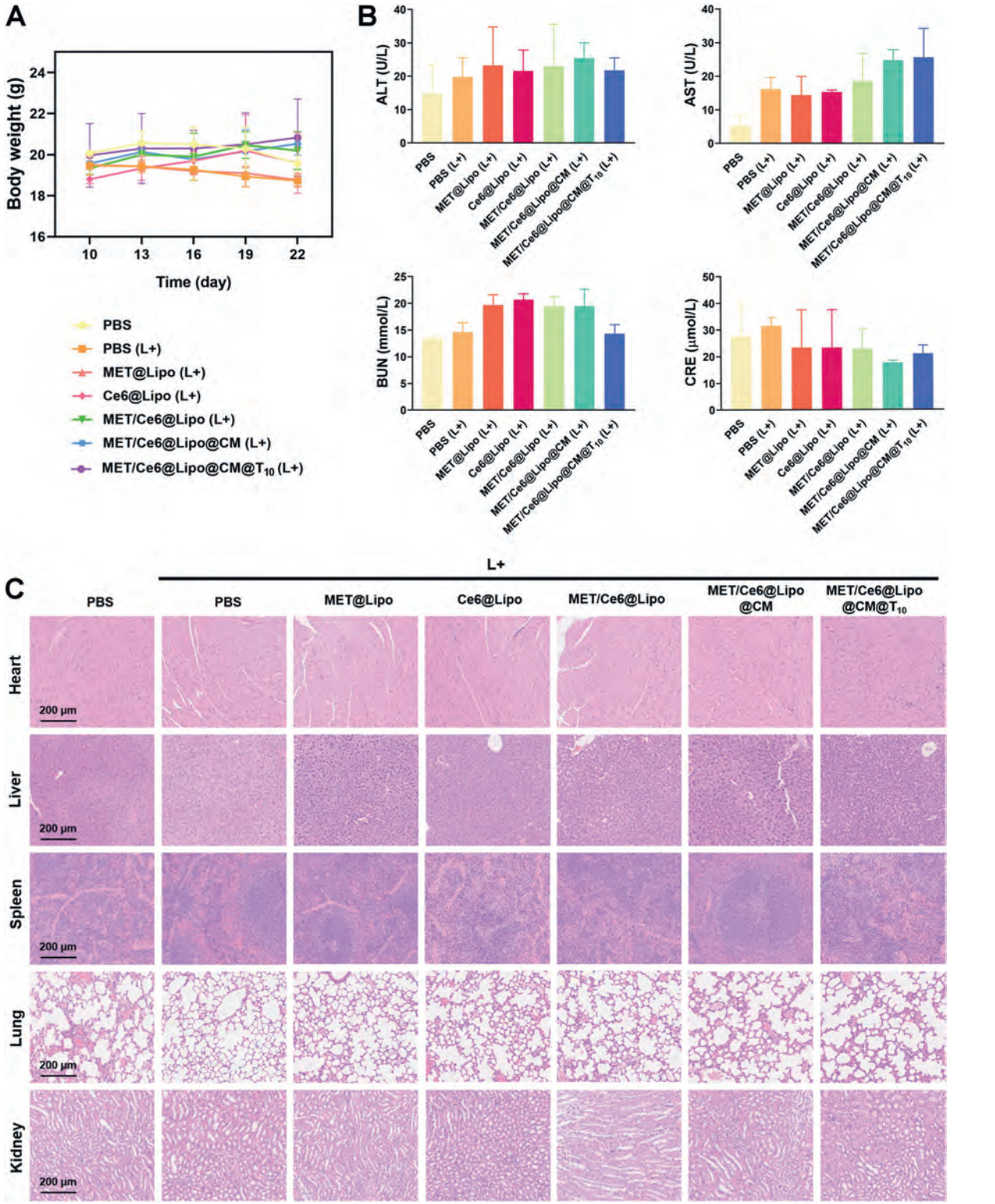

Figure 11 Biosafety evaluation of MET/Ce6@Lipo@CM@T_{10}. (A) Body weight of mice after different treatments. ($n = 3$). (B) ALT, AST, BUN, and CRE levels of serum from mice after various treatments ($n = 3$). (C) The H&E staining images of main organs (heart, liver, spleen, lung, and kidney) of mice at the end of different treatments.

normal range across groups, suggesting no significant liver or kidney damage caused by MET/Ce6@Lipo@CM@T_{10}. H&E staining of major organs (Fig. 11C) revealed no observable damage in the PBS, PBS(L+), MET@Lipo(L+), Ce6@Lipo(L+), MET/Ce6@Lipo(L+), MET/Ce6@Lipo@CM(L+), or MET/Ce6@Lipo@CM@T_{10}(L+) groups. This indicates that MET/Ce6@Lipo@CM@T_{10} (L+) exhibits excellent histocompatibility, with negligible toxicity to major organs, including the heart, liver,

spleen, lungs, kidneys, and brain. The results of body weight monitoring, biochemical analysis, and histopathology confirmed the safety and biocompatibility of this targeted nanosystem, demonstrating its potential for clinical development.

4. Conclusions

The BBB is a highly selective structure composed of cerebral microvascular endothelial cells, pericytes, and astrocytes, which regulate material transport between the blood and brain. Its tight junctions significantly restrict transendothelial transport, limiting the delivery of therapeutic agents to the brain and compromising treatment outcomes for brain diseases. To address this challenge, we designed a Tf-mediated biomimetic multifunctional lipo-complex co-loaded with Ce6 and MET. The developed lipo-complex demonstrated favorable physicochemical properties, storage stability, and safety. It achieved controlled drug release due to the dual-membrane protection provided by the liposome and CM. Surface modification with T_{10} enabled Tf binding, forming Tf-PCs, which facilitated binding to TfR overexpressed on tumor cells, thereby enhancing targeted drug delivery. *In vitro* studies showed that the co-delivery of MET and Ce6 significantly improved antitumor effects at the cellular level. *In vivo* imaging studies in tumor-bearing mice confirmed that Ce6@L-ipo@CM@T_{10} efficiently crossed the BBB *via* endocytosis, penetrated deep into brain tumors, and induced effective tumor cell apoptosis. MET alleviated hypoxia in tumor tissues, further enhancing the PDT efficacy of Ce6. The combined strategy of MET and PDT significantly inhibited tumor growth, as demonstrated by TUNEL fluorescence, HIF-1α staining, and H&E staining results. This study establishes a rational platform integrating PDT and immunoadjuvant therapy to enhance ROS production and immune responses. The lipo-complex exhibits endogenous protein ligand targeting and homologous cell homing capabilities, enabling efficient drug delivery to the brain and enhanced active targeting. These findings present a promising new approach for glioblastoma treatment.

Acknowledgments

This work was supported by the National Natural Science Foundation of China (82104106). CAMS in Innovation Fund for Medical Sciences (CIFMS) (2023-I2M-2-006, China). We thank LetPub editorial team (www.letpub.com.cn/)for language editing service.

Author contributions

Aihua Jin: conceptualization, methodology, investigation, formal analysis, writing - original draft. Nuoya Wang: methodology, formal analysis, writing - original draft. Yanhong Liu: methodology. Shuangqing Wang: writing - review & editing. Liqing Chen: investigation. Liming Gong: methodology. Wei Huang: writing - review & editing. Zhonggao Gao: writing - review & editing, supervision. Mingji Jin: methodology, investigation, writing - review & editing, supervision.

Conflicts of interest

The authors declare no conflicts of interest.

Appendix A. Supporting information

Supporting information to this article can be found online at https://doi.org/10.1016/j.apsb.2025.08.019.

References

1. Ruan HT, Chai ZL, Shen Q, Chen XS, Su BX, Xie C, et al. A novel peptide ligand RAP12 of LRP1 for glioma targeted drug delivery. *J Control Release* 2018;**279**:306−15.
2. Szopa W, Burley TA, Kramer-Marek G, Kaspera W. Diagnostic and therapeutic biomarkers in glioblastoma: current status and future perspectives. *BioMed Res Int* 2017;**2017**:8013575.
3. Tang W, Fan WP, Lau J, Deng LM, Shen ZY, Chen XY. Emerging blood−brain-barrier-crossing nanotechnology for brain cancer theranostics. *Chem Soc Rev* 2019;**48**:2967−3014.
4. Rominiyi O, Vanderlinden A, Clenton SJ, Bridgewater C, Al-Tamimi Y, Collis SJ. Tumour treating fields therapy for glioblastoma: current advances and future directions. *Br J Cancer* 2021;**124**:697−709.
5. Schaff LR, Mellinghoff IK. Glioblastoma and other primary brain malignancies in adults: a review. *JAMA* 2023;**329**:574−87.
6. Yang GQ, Liu Y, Chen JJ, Ding JX, Chen XS. Self-adaptive nanomaterials for rational drug delivery in cancer therapy. *Acc Mater Res* 2022;**3**:1232−47.
7. Blanco E, Shen H, Ferrari M. Principles of nanoparticle design for overcoming biological barriers to drug delivery. *Nat Biotechnol* 2015; **33**:941−51.
8. Butcher NJ, Mortimer GM, Minchin RF. Drug delivery: unravelling the stealth effect. *Nat Nanotechnol* 2016;**11**:310−1.
9. Zhou YQ, Peng ZL, Seven ES, Leblanc RM. Crossing the blood−brain barrier with nanoparticles. *J Control Release* 2018;**270**:290−303.
10. Zhang WS, Mehta A, Tong ZQ, Esser L, Voelcker NH. Development of polymeric nanoparticles for blood−brain barrier transfer-strategies and challenges. *Adv Sci* 2021;**8**:2003937.
11. Liao J, Gong LD, Xu QQ, Wang JY, Yang YY, Zhang SM, et al. Revolutionizing neurocare: biomimetic nanodelivery *via* cell membranes. *Adv Mater* 2024;**36**:e2402445.
12. Chen L, Hong WQ, Ren WY, Xu T, Qian ZY, He ZY. Recent progress in targeted delivery vectors based on biomimetic nanoparticles. *Signal Transduct Target Ther* 2021;**6**:225.
13. Wu SK, Tsai CL, Huang YX, Hynynen K. Focused ultrasound and microbubbles-mediated drug delivery to brain tumor. *Pharmaceutics* 2020;**13**:15.
14. Niu WB, Xiao Q, Wang XJ, Zhu JQ, Li JH, Liang XM, et al. A biomimetic drug delivery system by integrating grapefruit extracellular vesicles and doxorubicin-loaded heparin-based nanoparticles for glioma therapy. *Nano Lett* 2021;**21**:1484−92.
15. Liu YH, Wu H, Wang SQ, Zhang XT, Gong LM, Xiao CC, et al. Biomimetic multifunctional nanodrugs enable regulating abnormal tumor metabolism and amplifying PDT-induced immunotherapy for synergistically enhanced tumor ablation. *Mater Today* 2023;**68**: 125−47.
16. Kelly PM, Åberg C, Polo E, O'Connell A, Cookman J, Fallon J, et al. Mapping protein binding sites on the biomolecular corona of nanoparticles. *Nat Nanotechnol* 2015;**10**:472−9.
17. Xiao W, Wang YZ, Zhang HL, Liu YW, Xie R, He XQ, et al. The protein corona hampers the transcytosis of transferrin-modified nanoparticles through blood−brain barrier and attenuates their targeting ability to brain tumor. *Biomaterials* 2021;**274**:120888.
18. Ke PC, Lin SJ, Parak WJ, Davis TP, Caruso F. A decade of the protein corona. *ACS Nano* 2017;**11**:11773−6.
19. Oh JY, Kim HS, Palanikumar L, Go EM, Jana B, Park SA, et al. Cloaking nanoparticles with protein corona shield for targeted drug delivery. *Nat Commun* 2018;**9**:4548.
20. Mahmoudi M, Landry MP, Moore A, Coreas R. The protein corona from nanomedicine to environmental science. *Nat Rev Mater* 2023;**24**: 1−17.

21. Xiao W, Gao HL. The impact of protein corona on the behavior and targeting capability of nanoparticle-based delivery system. *Int J Pharm* 2018;**552**:328−39.
22. Huo TT, Yang YF, Qian M, Jiang HL, Du YL, Zhang XY. Versatile hollow COF nanospheres *via* manipulating transferrin corona for precise glioma-targeted drug delivery. *Biomaterials* 2020;**260**:120305.
23. Habib S, Singh M. Angiopep-2-modified nanoparticles for brain-directed delivery of therapeutics: a review. *Polymers* 2022;**14**:712.
24. Mehdipour G, Wintrasiri MN, Ghasemi S. CPP-based bioactive drug delivery to penetrate the blood−brain barrier: a potential therapy for glioblastoma multiforme. *Curr Drug Targets* 2022;**23**:719−28.
25. Ruan SB, Yuan MQ, Zhang L, Hu GL, Chen JT, Cun XL, et al. Tumor microenvironment sensitive doxorubicin delivery and release to glioma using angiopep-2 decorated gold nanoparticles. *Biomaterials* 2015;**37**:425−35.
26. Wu DD, Chen XH, Zhou SQ, Li B. Reactive oxidative species (ROS)-based nanomedicine for BBB crossing and glioma treatment: current status and future directions. *Front Immunol* 2023;**14**:1241791.
27. Cheng KM, Guo Q, Shen ZF, Yang WG, Wang YL, Sun ZJ, et al. Bibliometric analysis of global research on cancer photodynamic therapy: focus on nano-related research. *Front Pharmacol* 2022;**13**: 927219.
28. Chilakamarthi U, Giribabu L. Photodynamic therapy: past, present and future. *Chem Rec* 2017;**17**:775−802.
29. Ji B, Wei MJ, Yang B. Recent advances in nanomedicines for photodynamic therapy (PDT)-driven cancer immunotherapy. *Theranostics* 2022;**12**:434−58.
30. Liu ZY, Xie ZJ, Li WT, Wu XQ, Jiang XF, Li GH, et al. Photodynamic immunotherapy of cancers based on nanotechnology: recent advances and future challenges. *J Nanobiotechnol* 2021;**19**:160.
31. Wei X, Song MZ, Jiang GR, Liang M, Chen CL, Yang ZY, et al. Progress in advanced nanotherapeutics for enhanced photodynamic immunotherapy of tumor. *Theranostics* 2022;**12**:5272−98.
32. Zhao M, Yang XP, Fu H, Chen CR, Zhang YH, Wu ZH, et al. Immune/hypoxic tumor microenvironment regulation-enhanced photodynamic treatment realized by pH-responsive phase transition-targeting nanobubbles. *ACS Appl Mater Interfaces* 2021;**13**: 32763−79.
33. Xiong W, Qi L, Jiang N, Zhao Q, Chen LX, Jiang X, et al. Metformin liposome-mediated PD-L1 downregulation for amplifying the photodynamic immunotherapy efficacy. *ACS Appl Mater Interfaces* 2021; **13**:8026−41.
34. Xie W, Deng WW, Zan MH, Rao L, Yu GT, Zhu DM, et al. Cancer cell membrane camouflaged nanoparticles to realize starvation therapy together with checkpoint blockades for enhancing cancer therapy. *ACS Nano* 2019;**13**:2849−57.
35. Hadjidemetriou M, Al-Ahmady Z, Mazza M, Collins RF, Dawson K, Kostarelos K. *In vivo* biomolecule corona around blood-circulating, clinically used and antibody-targeted lipid bilayer nanoscale vesicles. *ACS Nano* 2015;**9**:8142−56.
36. Franke H, Galla H, Beuckmann CT. Primary cultures of brain microvessel endothelial cells: a valid and flexible model to study drug transport through the blood−brain barrier *in vitro*. *Brain Res Protoc* 2000;**5**:248−56.
37. Yang GB, Phua SZF, Lim WQ, Zhang R, Feng LZ, Liu G, et al. A hypoxia-responsive albumin-based nanosystem for deep tumor penetration and excellent therapeutic efficacy. *Adv Mater* 2019;**31**: e1901513.
38. Hu C, Zhuang WH, Yu T, Chen L, Liang Z, Li GC, et al. Multi-stimuli responsive polymeric prodrug micelles for combined chemotherapy and photodynamic therapy. *J Mater Chem B* 2020;**8**:5267−79.
39. Peng N, Yu H, Yu WJ, Yang MA, Chen HX, Zou T, et al. Sequential-targeting nanocarriers with pH-controlled charge reversal for enhanced mitochondria-located photodynamic-immunotherapy of cancer. *Acta Biomater* 2020;**105**:223−38.
40. Wheaton WW, Weinberg SE, Hamanaka RB, Soberanes S, Sullivan LB, Anso E, et al. Metformin inhibits mitochondrial complex I of cancer cells to reduce tumorigenesis. *eLife* 2014;**3**:e02242.
41. Yang ZY, Wang JF, Liu S, Li XH, Miao LY, Yang B, et al. Defeating relapsed and refractory malignancies through a nano-enabled mitochondria-mediated respiratory inhibition and damage pathway. *Biomaterials* 2020;**229**:119580.
42. Zannella VE, Dal Pra A, Muaddi H, McKee TD, Stapleton S, Sykes J, et al. Reprogramming metabolism with metformin improves tumor oxygenation and radiotherapy response. *Clin Cancer Res* 2013;**19**:6741−50.
43. Wang L, Hu Y, Hao Y, Li L, Zheng C, Zhao H, et al. Tumor-targeting core−shell structured nanoparticles for drug procedural controlled release and cancer sonodynamic combined therapy. *J Control Release* 2018;**286**:74−84.
44. Shao Q, Morgounova E, Jiang C, Choi J, Bischof J, Ashkenazi S. *In vivo* photoacoustic lifetime imaging of tumor hypoxia in small animals. *J Biomed Opt* 2013;**18**:076019.
45. Rich LJ, Seshadri M. Photoacoustic imaging of vascular hemodynamics: validation with blood oxygenation level-dependent MR imaging. *Radiology* 2015;**275**:110−8.
46. Krysko DV, Garg AD, Kaczmarek A, Krysko O, Agostinis P, Vandenabeele P. Immunogenic cell death and DAMPs in cancer therapy. *Nat Rev Cancer* 2012;**12**:860−75.
47. Banerjee SS, Paul D, Bhansali SG, Aher ND, Jalota-Badhwar A, Khandare J. Enhancing surface interactions with colon cancer cells on a transferrin-conjugated 3D nanostructured substrate. *Small* 2012;**8**: 1657−63.
48. Qiu S, Liu JH, Chen JM, Li YN, Bu T, Li ZL, et al. Targeted delivery of MerTK protein *via* cell membrane engineered nanoparticle enhances efferocytosis and attenuates atherosclerosis in diabetic ApoE$^{-/-}$ mice. *J Nanobiotechnol* 2024;**22**:178.
49. Srinivasan B, Kolli AR, Esch MB, Abaci HE, Shuler ML, Hickman JJ. TEER measurement techniques for *in vitro* barrier model systems. *J Lab Autom* 2015;**20**:107−26.
50. Luk BT, Zhang L. Cell membrane-camouflaged nanoparticles for drug delivery. *J Control Release* 2015;**220**:600−7.
51. Ge J, Zuo MM, Wang QR, Li Z. Near-infrared light triggered *in situ* release of CO for enhanced therapy of glioblastoma. *J Nanobiotechnol* 2023;**21**:48.
52. Zhang WG, Kang MM, Li X, Pan YZ, Li ZR, Zhang YB, et al. Fiber optic-mediated type I photodynamic therapy of brain glioblastoma based on an aggregation-induced emission photosensitizer. *Adv Mater* 2024;**36**:e2410142.
53. Yi H, Ghosh D, Ham MH, Qi J, Barone PW, Strano MS, et al. M13 phage-functionalized single-walled carbon nanotubes as nanoprobes for second near-infrared window fluorescence imaging of targeted tumors. *Nano Lett* 2012;**12**:1176−83.
54. Wang R, Li XM, Zhou L, Zhang F. Epitaxial seeded growth of rare-earth nanocrystals with efficient 800 nm near-infrared to 1525 nm short-wavelength infrared downconversion photoluminescence for *in vivo* bioimaging. *Angew Chem Int Ed Engl* 2014;**53**:12086−90.